Fundamentals of Power Systems Modelling in the Presence of Converter-Interfaced Generation

Mario Paolone
École Polytehcnique Fédérale de Lausanne
Distributed Electrical Systems Laboratory
Lausanne, Switzerland
mario.paolone@epfl.ch

Antonello Monti
RWTH Aachen University
Institute for Automation of Complex Power Systems
Aachen, Germany
amonti@eonerc.rwth-aachen.de

Trevor Gaunt
University of Cape Town
Department of Electrical Engineering
Cape Town, South Africa
ct.gaunt@uct.ac.za

Thierry Van Cutsem
University of Liège
Fund for Scientific Research (FNRS)
Liège, Belgium
t.vancutsem@uliege.be

Xavier Guillaud
Univ. Lille, Arts et Metiers Institute of Technology, Centrale Lille, Yncrea Hauts-de-France, ULR 2697 - L2EP, F-59000
Lille, France
xavier.guillaud@centralelille.fr

Vijay Vittal
Arizona State University
School of Electrical, Computer and Energy Engineering
Tempe, AZ, USA
vijay.vittal@asu.edu

Marco Liserre
University of Kiel
Chair of Power Electronics
Kiel, Germany
ml@tf.uni-kiel.de

Costas Vournas
National Technical University of Athens
School of Electrical and Computer Engineering
Athens, Greece
vournas@power.ece.ntua.gr

Sakis Meliopoulos
Georgia Institute of Technology
School of Electrical and Computer Engineering
Atlanta, GA, USA
sakis.m@gatech.edu

***Abstract*— This survey paper discusses the fundamentals of power systems modelling in the presence of large amounts of converter-interfaced generation (CIG). By referring to real-life events characterised by anomalous dynamics associated to the presence of CIG, the concepts of narrow versus broad band signals are first recalled along with the limitation of the meaning of apparent power, power factor and reactive power. In this regard, the adequacy of the phasor representation of voltages and currents waveforms is thoroughly discussed. Then, with respect to the central subject of control of power converters, a revised definition of grid-following and grid-forming converters is provided along with a thorough discussion of their associated controls and a comprehensive classification for both classes of converters. Several applications inspired by actual case studies are included in the paper in order to provide realistic application examples.**

***Index Terms*—Power systems analysis, modelling, signal processing, power electronics, distributed generation, control.**

I. Introduction

It is well known that power systems are large, nonlinear, multi-time-scale, hybrid (discrete-continuous) and complex systems. As such, they are usually analysed for specific problems with relatively simplified models under appropriate assumptions. One of the most common of such assumptions when dealing with large power system stability dynamics is the *quasi-sinusoidal state*. In other words, power system dynamics taking place within time windows from less than a second to several seconds are represented by time-varying voltage and current phasors. As explained further below, this very reasonable hypothesis is based on the assumption that synchronous generators are the dominant dynamic component of the power system. On the other hand, *electromagnetic transient models* rely on far more detailed representation solving the underlying electrical circuits' differential equations with no a-priori assumption on the quasi-sinusoidal state of the system. They are usually used for smaller systems and/or for

relatively short simulation time windows where high-fidelity on the voltage/current waveforms is needed.

The increased penetration of converter-based renewable power sources and HVDC in power systems challenges the above decomposition of power system studies into phasor-based vs electromagnetic-transient-based, so that intermediate solutions are becoming necessary in several cases. Indeed, it is now conceivable that a large percentage of generation in a power system may not be based on synchronous generators and thus the dominant dynamics may change [1] as already documented by system operators [2-4]. This situation could trigger larger frequency excursions and much faster control actions that affect the shape of the voltage and current waveforms resulting in the phasor approximation introducing too large approximations. Naturally, the phasor approximation will still valid for steady-state power systems studies and may be revised when dealing with time-domain power systems models coupled with the design of converter-interfaced generation (CIG) controls.

At the same time, there is a significant research activity into the dynamics, control and stability of systems with significant penetration of CIG, i.e. power generation systems connected to the electric grid by means of fully controllable power converters (e.g., [5]) and HVDC systems. While many publications deal with the impact of decreasing system inertia [6-8] or low short-circuit ratios in weak areas [9], relatively fewer have discussed in detail the converter control laws (e.g. [10-13]) along with analysing the interaction of several, high-capacity converters located close to each other and connected with transmission lines.

With respect to other surveys, e.g., [8, 14-17], this paper has the goal to discuss specific aspects related to the fundamentals of power systems modelling in the presence of large amount of CIG. In this respect, section II is devoted to the modelling needs: it focuses on the problem of power systems' reduced inertia, recalls the concepts of narrow versus broad band signals and discusses the interaction between CIG and synchronous machine controls and the limitation of the concepts of apparent power, power factor and reactive power. In addition, as the increased penetration of CIG challenges legacy protection systems, the section discusses the potential mis-operation of protection systems. Then, section III illustrates several real-life events characterised by anomalous dynamics associated to the presence of CIG. Section IV discusses in detail the adequacy of the phasor representation of voltage and current waveforms usually adopted in power systems. In particular, this section illustrates the representation limits of phasors in the presence of broad-band signals, it discusses the behaviour of the largely adopted Park transform in the presence of broad-band signals and, then, inspired by the theory on analytic signals, the section discusses two approaches to model broad-band signals beyond the concept of static phasors. Section V is devoted to discuss converters' control. The section first provides revised definitions of grid-following and grid-forming power-electronics-based units in large grids. Then, it discusses the power controls of both grid-forming and grid-following converters, providing a relevant classification for both classes and examples. Section VI shows and discusses application examples with respect to the modelling aspects discussed in the previous sections of the paper. The main goal of this section is to make reference to application examples associated to power systems of significant size and complexity. Section VII provides the concluding remarks of this survey paper.

II. SELECTED NEEDS IN POWER SYSTEMS MODELLING IN THE PRESENCE OF CIG

A. Interaction of CIG and synchronous machine controls

Traditionally, power system dynamics are associated with synchronous generators and their controls responsible to maintain frequency and voltage through speed governors (for active power control) and automatic voltage regulators (for reactive power control). The increased penetration of CIG has a considerable impact on these controls. In the first place, the reduced capacity of synchronous generators poses a challenge on the efficiency of their controls to maintain proper standards in frequency and voltage. It is thus required that the CIG should participate in system controls [1]. At this point it becomes essential to distinguish the radically different ways in which conventional and CIG can handle system frequency and voltage controls. These differences become important as the participation of both types of generation becomes comparable and, eventually, the system transitions from primarily synchronous-machine-based to mostly converter-based systems.

In synchronous machines, the frequency is linked to the rotor speed (ω) and the associated moment of inertia (J) and kinetic energy (E_k) of the rotating mass. System load variation is initially served through this kinetic energy creating a frequency transient sensed by the speed governors that adjust the mechanical power to match the electric load and thus restoring frequency close to its nominal value (secondary frequency regulation acts much later and it does not affect the initial response). Due to the high inertia of synchronous machines, system frequency variations remain limited in interconnected systems, thus allowing a phasor approximation for most transients without considerable error.

CIG has a much smaller reservoir of energy in the form of electric field energy (E_{dc}) stored in the converter DC side voltage (V) and capacitance (C). Thus, the equivalent to AC frequency (rotational speed) for active power control (load balancing), is the DC voltage. The respective energy formulae are recalled here below.

$$E_k = \frac{1}{2} J\omega^2 \qquad E_{DC} = \frac{1}{2} CV^2 \tag{1}$$

Usually the stored energy for each device is normalized as the ratio of energy over rated power (say P_N) and is thus expressed in seconds: $H = E/P_N$. Whereas for synchronous machines H has a value of 3-5s, for CIGs the corresponding value is in the order of milliseconds.

For primary frequency control, the essential dynamics are those of conventional generator prime mover controls, since renewable energy resources (RESs), such as wind and

photovoltaic, need to either operate de-loaded (thus continuously spilling energy) or rely on energy storage, such as batteries, when needing to increase their generation to meet load.

Voltage regulation is very similar in synchronous generators and CIG. The main difference is the limiting conditions under which voltage control is no longer possible. In synchronous generators this is a complex process involving over-excitation and under-excitation limiters. In CIG, the limits are set by the maximum converter current and are thus dependent on active power generation and nominal power factor. Due to their distributed nature, CIG can provide several valuable ancillary services through their voltage/reactive power control that include, but are not limited to, local voltage support, reactive power support for voltage stability enhancement, active and reactive load modulation.

The damping of electromechanical oscillations between synchronous generators (small signal rotor angle stability) is influenced by voltage regulation, thus also by CIG when present. In cases of unstable oscillations, power system stabilizers of synchronous generators can be replaced by similar converter controllers modulating active and/or reactive power [18].

B. Reduced inertia

As already discussed above, the fundamental change brought by the adoption of RERs is the replacement of synchronous machines with power electronic interfaced devices. This concept obviously applies to photovoltaic generation but also to wind turbines where the current trend is to adopt the so-called full-converter solutions [19]. Such a transformation has two types of consequences.

- The early response of the system is driven by the characteristics of the closed loop control of the CIG while, in the past, it was determined by the natural response of the synchronous machines.
- The design of the power converters' controls determines the system dynamics (in particular, the system frequency) as well as the inertial response of the system with respect to the frequency dynamics.

In the traditional approaches adopted to model power systems, the response of the system was considered to be driven by the (large) inertia of the synchronous machines able to significantly filter (or limit) the rate-of-change-of-frequency (RoCoF) and the corresponding frequency nadir in case of contingencies. In power systems where the majority of the power generation is provided by power electronic converters, this behaviour depends on the converter control characteristics.

In case the converters are designed to be *frequency followers*, their inherent contribution to the system inertia is null as the converters simply adapt to the frequency of the system as determined by other generators. However, it is possible to adjust the active power with respect to the frequency derivative to mimic an inertial effect [20] even though the amount of available energy reserve of CIGs is limited as discussed in the previous subsection. The device can offer *inertial support* by deriving energy from an auxiliary source making use of very fast converter controls, which are essentially keeping the DC voltage constant. Such an auxiliary energy source can be the kinetic energy of a wind turbine generators asynchronously connected through the converter. It should be noted, however, that this response is limited by the allowable excursion of speed of the wind turbine shaft and is influenced by other wind generator controls, such as the maximum power tracking as well as the power rating of the converter [21-23]. Furthermore, as pointed out in [24], the frequency measurement filtering may largely mitigate this inertial effect. Other devices may use supercapacitors for the same service. The resulting available inertial response of CIG can be useful in a first stage of synchronous machines replacement in order to compensate for the system loss of inertia. In particular, the use of converters capable of operating as *grid-forming* devices, has been advocated as a possible means to go beyond a mere mitigation of the problems caused by decreased inertia. In fact, the new degrees of freedom offered by these devices allow for the re-design of power systems controls introducing a new paradigm for operation and control aspects [25]. Thus, for very large penetration of CIGs, a radically different active power control is possible without relying on the rotating mass inertia to keep system energy balance. In such cases, frequency (which can still be used as the proxy signal for sharing active power) may become much more volatile without affecting the security of service. In this respect, the transient current and voltage AC waveforms are expected to be severely modified in the foreseeable future making the used phasor approximations questionable.

C. Narrow vs broad-band signals

In order to have a clear understanding of the difference between *narrow-* and *broad-band signals*, it is worth defining their characteristics. *Narrow band signals* are characterised by a discrete spectrum where the energy is concentrated in a single frequency component; therefore, their bandwidth is zero. *Broad-band signals* are instead characterised by a continuous spectrum of generic bandwidth and their energy cannot be computed by adding the energy of a finite set (i.e., bins) of signal components.

During electromechanical transients in power systems triggered by large contingencies, the electrical power may be transmitted over a continuous spectrum that is no longer concentrated on the sole fundamental component [26] (i.e., a narrow band signal, see section IV.A for further details). Therefore, traditional modelling approaches relying on the phasor representation derived from the *Fourier Transform* (FT) may exhibit limits to properly identify the characteristics of signals associated to power grid voltages and currents, as well as the associated transmitted/injected powers. This shortcoming is essentially due to the fact that the FT is projecting the analysed signals over a functional basis uniquely composed by steady-state sinusoidal functions. The literature on signal processing (e.g. [27]) has addressed this limitation by the *theory of analytic signals* suitably coupled with a more generic transformation like the *Hilbert transform* (HT).

With the intent to provide to the reader a different perspective with respect to the use of the traditional phasor modelling approach, sections IV.A, IV.B and IV.E provide a comprehensive discussion on the analysis of signals representative of operating conditions of modern power grids when analysed using the two above-mentioned techniques.

D. On the meaning of apparent power and power factor

An important concept in measurement theory is that representational measurements need to be based on the physical components being measured [28] and complying with all the principles and laws of engineering science. Since few power theory models consider explicitly the voltage change at the receiving end of a delivery system as a result of compensation, or do not address directly the waveform distortion by harmonics components that can be considered as superimposed sinusoidal waveforms [29], they cannot approach being representational measurements. The measurement of reactive power in real systems is particularly problematic [30], delivering no net energy in a fundamental frequency wavelength, taking a non-physical unit (VArs) and relying on a non-physical geometric model for its definition in terms of power and apparent power [31].

It has been shown [32] that compensation by a power electronics compensator or inverter, can be by current transfer from one wire to another (instantaneous power) and/or by storage and return of current from and back into a wire within the duration of a wavelength. A subsequent paper [33] showed that conforming to engineering laws requires all system potentials to be referred to a common frame of reference. Another approach, based on applying the HT and independent of the concept of reactive power, identifies the adaptive compensation required as a result of the changed load voltage [34].

Steady-state analysis of a power system can be simplified by using superposition of its Thévenin equivalent circuits and several techniques are available to measure or derive the Thévenin parameters. Applying the possibility of compensation of a load at a point of common coupling (PCC) of an m-wire network with a finite number of h harmonic components and represented by its Thévenin equivalents, provides for transfer not only between the wires but also between harmonics. Rigorous compliance with Kirchhoff's voltage and current laws can be maintained using linear algebra in the Hilbert space, projecting orthogonally one vector onto another. The currents $I_{S,h}$ in the lines without (or before) compensation can be resolved into the active current components $I_{A,h}$ in phase with their respective voltages $V_{Th,h}$ at the Thévenin point, and all other current components $I_{C,h}$. Then, the magnitude of the power sent out is $\|\boldsymbol{V}_{Th}'\|\|\boldsymbol{I}_A'\|$ and the apparent power S of the power system is calculated as $\|\boldsymbol{V}_{Th}'\|\|\boldsymbol{I}_S'\|$, where $\|\boldsymbol{V}_{Th}'\|$ is the resistance-weighted voltage vector at the Thévenin point and $\|\boldsymbol{I}_S'\|$ is the norm of resistance-weighted current vector without compensation [32]. The power system and approach to measurement are illustrated in Fig. 1.

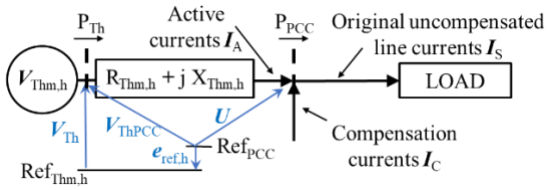

Figure 1. Identifying power and apparent power in the Thévenin equivalent of an *m*-wire power system with waveform distortion by harmonics *h*.

The loss incurred by delivering only I_A from the source to the PCC is the minimum possible loss, and the total loss of delivering $\boldsymbol{I}_S = \boldsymbol{I}_A + \boldsymbol{I}_C$ comprises the minimum loss and the avoidable loss that can be eliminated by compensation. Then the power factor $pf = P/S$ is also the index of the losses without or before compensation of the power system supplying the load at the PCC, $pf = \|\boldsymbol{I}_A'\|/\|\boldsymbol{I}_S'\|$, and after compensation the $pf = 1$.

The change in delivery losses by compensation is not given simply by the loss component associated with $\boldsymbol{I}_C$ since $\|\boldsymbol{I}_S'\|^2 = \|\boldsymbol{I}_A'\|^2 + \|\boldsymbol{I}_C'\|^2 + 2 < \boldsymbol{I}_A', \boldsymbol{I}_C' >$ and in most cases the term $2 < \boldsymbol{I}_A', \boldsymbol{I}_C' >$ has real value (in Watts), with the implication that the vectors are not orthogonal, else the value would be zero.

The calculations of power delivered and power loss are based entirely on measurements at the PCC of wire voltages and currents and the Thévenin equivalent impedances. The calculations are done easily for multi-wire systems using linear algebra, with rigorous attention to the reference points of voltage measurements, especially from a common null reference at the Thévenin point.

This approach identifies the apparent power as the active power that, for the same losses, could be dispatched from or delivered to the Thévenin point by injecting into or drawing from the power system the optimum line currents. Accordingly, apparent power has the same unit, Watt, as active power, which resolves an inconsistency in the conventional definition using a power triangle.

Further, conventional reactive power is defined only for fundamental frequency, sinusoidal (steady state) signals in a single phase or balanced 3-phase system with negligible delivery system resistances and inductances, and is inconsistent with the definitions of power factor and apparent power in the general case. Therefore, it is quite likely that power system simulation or control based on reactive power as conventionally defined or calculated might give results and responses that are inconsistent with a physical model of the power system.

This general power theory [35] can be applied to unbalanced systems in the presence of phase displacement and harmonic distortion, even to a multi-wire DC system, and hybrid AC and DC systems.

Use-cases include the injection of power into an unbalanced network, as is common with distributed generation at low and medium voltage levels. It can be shown that injection of equal currents at conventionally defined pf into a feeder unbalanced by intermediate loads does not always incur the minimum

delivery loss. Instead, the optimum injection of currents by an inverter-based source eliminates the avoidable loss and achieves delivery with the minimum loss.

In addition to converter applications, this new approach to identifying active currents, power factor and apparent power opens up new possibilities in compensator and inverter design, power system analysis, metering and tariffs, the revision of standards documents, and in education and research.

E. Impact on existing protection schemes

As more CIG is supplying electricity to the power system, the legacy protection and control systems have become inadequate. Already, some relay mis-operations have been reported in the vicinity of utility size wind and PV farms. The reason for this is that conventional generators have fundamentally different fault characteristics than CIG. Inverter fault currents are primarily determined by inverter controls. First, inverters limit the fault current to values comparable to max load current. As a matter of fact, field data show that the fault current level depends on wind and solar conditions during the fault and in some cases the fault current may be lower than the nominal load current [36]. Oversizing inverters can provide higher fault currents, assuming there is storage, but there is an economic and practical limit to this. In addition, the duration of the fault current provided by inverters is limited to the first two cycles and then reduces to a value practically identical to the maximum load current. The reduced fault currents make the conventional over-current protection schemes unreliable and difficult to coordinate. Many other protection functions depend on a large separation between max load current and fault current for proper coordination and reliable protection, i.e. directional overcurrent, impedance protection, and other such protection schemes. In addition, many protection functions require detection of fault direction (such as directional overcurrent, distance protection). These relays require a polarizing quantity that is present at sufficient value during the fault. In conventional systems, negative or zero sequence components provide a reliable polarizing quantity. Inverters, on the other hand, do not produce zero sequence and the negative sequence components since they are suppressed by inverter controls. Lack of zero/negative sequence components will lead to malfunctioning of these relays. Negative sequence current control in wind turbines interferes with the proper functioning of conventional protection devices [37]. Some, phase balance relays use the negative sequence quantities to detect unbalanced faults. These relays will mis-operate if generation sources are inverter interfaced generation [38]. It has been shown that power swing blocking relays and out-of-step protection will mis-operate in the vicinity of wind-generation interfaced with inverters to the power system [39]. Reference [40] summarizes the effects on conventional protection due to the lack of negative sequence components in inverter fault currents. Some countries try to address this issue by including in national norms the requirement that inverters should produce negative sequence quantities during a fault. We believe this measure must be a temporary measure; the engineering community should seek better protection methods that are immune to the inverter fault current characteristics and we offer a proposal later on in this paper.

Another reality in systems with high penetration of CIG is that the system topology will be changing much more often and more drastically than in conventional systems due to the variability of renewable resources that are behind the inverters. If a protection scheme is designed to coordinate well with other protection schemes for a particular network topology, it may not be well coordinated if there is a drastic topology change. To cope with these issues different approaches have been proposed: model-based adaptive relaying, incremental distance, traveling wave, active power line carrier, and others. Yet these approaches have not been tested under real field conditions and more importantly they do not address the impact of inverter interfaced generation. Model-based adaptive relaying is promising but present proposals are very complex since they require a sophisticated infrastructure to monitor the conditions and changes in the system and depend on use of legacy protection functions [41]. Specifically, they seek to change the settings of legacy protection functions according to prevailing conditions. This approach inherits all the shortcomings of legacy protection when applied to systems with high penetration of CIGs. The complexity brings into question the ability to re-coordinate relay settings with the required speed once a network condition has changed. In addition, there exist several protection gaps with or without the presence of CIGs. For example, we do not have 100% reliable protection for down conductors/high impedance faults [42]; distributed CIGs make the problem more complex as they provide additional backfeed to keep the down conductor energized creating serious safety concerns. In distribution systems, millions of inverters interfaced distributed generation units such as photovoltaic (PV) systems will be integrated into the power grid. This paradigm shift in the operation of power distribution systems causes bidirectional power flows and low short circuit current generation. Therefore, conventional over-current protection schemes will not be effective solutions anymore [43]. Several methods have been proposed to address the problem, some of which are discussed in [44]. For instance, distance/impedance protection is utilized for power distribution systems with distributed generation in [45]. However, distance relays face difficulties in power distribution systems with short lines, dynamically changing in-feeds from installed PV systems and substantially unbalanced lines. Some of the challenges of application of distance protection for power distribution systems are discussed in [46]. The directional over-current relay with adaptive settings is another possible approach [47]. However, they may fail to operate in the case of fault scenarios that generate low short circuit currents, specifically when multiple microgrids connected to the distribution system operate in the islanded mode. Communication-assisted protection schemes have also been proposed to operate either based on the pilot protection strategy or differential protection strategy. In schemes based on the pilot protection strategy such as [48] directional relays exchange the local decisions with other relays to make the final decision. These protection schemes may fail to operate correctly in the case of low short circuit currents or lack of negative sequence components in the

fault currents. In schemes based on the differential protection strategy such as [49] the sampled values are exchanged, and each relay makes the final decision based on the collected sampled values. Although this strategy is more sensitive to the short circuit compared to the pilot protection strategy, it still operates based on pre-defined settings. Therefore, only fault scenarios that generate over-currents larger than the threshold values can be detected. Also, these schemes require frequent update of the setting values upon the change in the topology of the network. In summary, proposed schemes are complex, they do not appear to meet the time requirements for effective protection (need decisions in a few cycles) and they do not address the new challenges that have been created by the fault current characteristics of CIG. Recent concerns for cyber security necessitate that the protection and control system must be also cyber secure. New approaches are needed that will remove protection gaps, provide a robust and cyber-secure protection and control system for systems with high penetration of inverter interfaced generation.

F. Interaction among CIG and power systems stability

CIG is characterized by different control layers: inner control layers (PWM and typically current control), medium control layers (transformations and synchronization) and external control layers (control of dc and ac voltages) as shown in Fig. 2 with an indication of the approximate frequency range of operation in relation to the fundamental AC frequency f_1 and power converter switching frequency f_s.

Once assumed that these layers are correctly designed to be stable also when they operate all together (i.e. that no unstable interactions arise among them), the connection of the power converter to the electric grid, where other power converters are connected together with electrical machines which constitute classical components of the grid, can give rise to new stability challenges as well as impact classical power system stability. These issues are briefly reviewed in the following not in the microgrid perspective, as done in [50], and consequently not in the perspective of a fully power-electronic-powered-grid but in the context of a bulk power system with growing converter-based generation. In this sense the control layers of different power converters interact among them through the grid [51], which is still a system stability problem. The power converter control loops impact also voltage, angle and frequency stability, i.e. classical power system stability issues. It is worth noting that a significant difference between the stability scenarios of a microgrid and of the bulk power system is that in this second case the interaction with synchronous-based generation will be dominantly of concern.

In fact, the multiple-timescale control systems of power electronic converters will impact the converter and system stability, when connected to the electric grid, by cross couplings with electromechanical dynamics of electrical machines and the electromagnetic transients of other power converters connected nearby and the power network itself. As a consequence, abnormal resonances across a wide frequency range can occur [51].

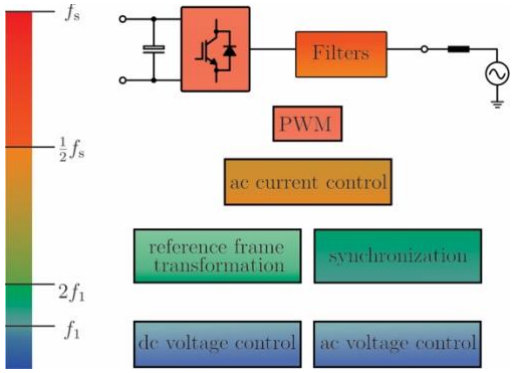

Figure 2. Different Control layers and their frequency of operation.

The small-signal dynamics of power electronic converters can potentially introduce negative damping in the power system [52], which in turn destabilizes the natural frequencies of the passive components in power system, leading to resonance instabilities. This phenomenon's frequency can vary from sub-synchronous to harmonics of several kHz, depending on the converters' control bandwidth and specific electric grid conditions [51].

The synchronization [53,54], and external control layers [55] may bring negative damping in the low frequency range, while the inner control layers impact on the stability in the high frequency range. The accurate analysis of resonance instabilities requires special attention to the modelling of power electronic converters and adapting it depending on the observed phenomenon [56].

The synchronization can impact the stability of microgrids [57] if the dynamics of the PLLs are slow (i.e., with low bandwidth). On the contrary in bulk power system it is reasonable to use PLLs with low bandwidth since they can well attenuate grid disturbances and the grid is not loaded as much as for the microgrid case. Nevertheless, the reaction time of grid connected converters might have a large impact on system stability in a different sense. The fault-ride-through behavior of converters has been largely debated in recent years, and especially the necessity for a fast-current injection during fault conditions. As an example, National Grid UK has recently requested to an expert group associated with the development of the UK grid code (GC100) to investigate new converter control strategies allowing almost instantaneous reaction ahead of the use of a dedicated synchronization unit. More specifically, a sufficient near instantaneous reactive current injection is requested in order to maintain the retained voltage to a sufficient level and ensuring network stability [58].

Fig. 3 conceptually explains the difference in the converter behaviour regarding current injection at the occurrence of a grid fault, shown in the reports provided by NGESO [58]. The dynamic behaviour of the converter labelled as virtual synchronous machine (VSM), and which will be discussed separately in this paper in section V, is compared to the response of a standard converter using a PLL. The reaction of the VSM (and generally of a grid-forming converter) to a grid fault is a consequence of the emulated behavior of voltage

source behind reactance, which results in a near to instantaneous injection of reactive power without the need for identification of the voltage phasor. On the contrary, state-of-the-art grid connected converters adopting PLLs or similar synchronization techniques, do introduce an unavoidable delay, due to the necessity for an accurate estimation of amplitude and phase of the instantaneous grid voltage for the proper injection of the required amount of current. Therefore, driven by the need for enhancing the performances of grid-connected converters in reducing their reaction time following a grid event, studies have shown that there are physical limitations to the highest PLL bandwidth of grid-following (GFL) converters [53,59]. To this extent, a trade-off for the design of PLL bandwidth has to be made between power quality and stability of the grid.

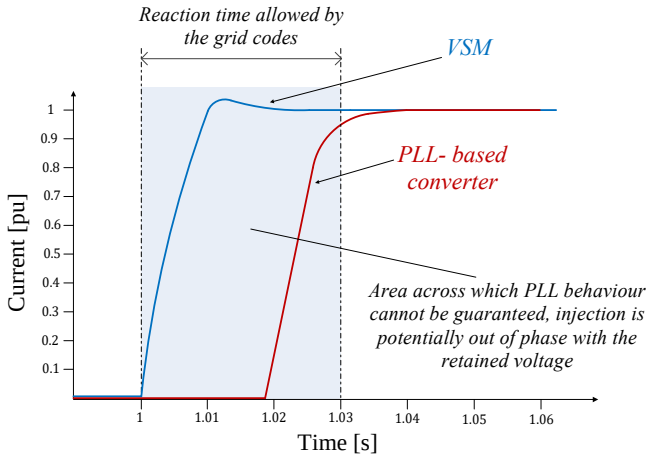

Figure 3. Different reaction times of converter control strategies investigated by NGESO [58].

The concept of grid-forming (GFM) converters, initially introduced for micro- and islanded grid applications, has been recently proposed for applications in wide interconnected systems, and it will be discussed in section V. Studies have shown that, in contrast to GFL converters using PLLs [53,59], power-synchronization based algorithms are particularly suitable for weak grid applications [60-62].

Even though this synchronization principle eliminates the need for a dedicated synchronization unit, and consequently of the stability issues caused by the PLL, large transient disturbances like grid faults, might cause instability typical of SMs such as angle instability. In fact, due to the intrinsic voltage source behavior of a GFM converter, the occurrence of a grid fault might provoke converter overcurrent, jeopardizing the integrity of the hardware components. The countermeasures taken for limiting converter currents might destabilize the power synchronization loop, due to the mismatch in the power balance caused by the unavoidable reduction of the maximum power that the converter is able to inject during the fault. Several techniques have been proposed in the literature in order to limit the maximum converter currents, and prevent the converter from instability issues by properly handling the behavior of the outer power synchronization loop under fault conditions [61,63,64]. The topic of current-limitation when grid-forming units are used to interface generation to the grid is a new topic which still needs to be deeply investigated and since no mature solution exist, it is expected that few of them will be proposed in the future years.

III. Real-life examples of power systems dynamics involving by CIG

This section illustrates real-life events characterised by anomalous power systems dynamics involving the presence of CIG. The events analysed here provide actual examples of the role that CIG may play in power systems behaviour subsequent to large disturbances and set the base for the quantitative analysis contained in sections IV, V and VI.

A. Event of September 28, 2016, Australia [3]

On September 28, 2016, multiple tornadoes in South Australia (SA) tripped multiple 275 kV transmission circuits, and resulted in multiple faults in quick succession. The series of voltage dips from the faults triggered protection on several wind farms to runback about 456 MW of wind generation. The reduction in wind farm output was compensated by an increase in power imported from Victoria (VIC) via the Heywood interconnector. However, the Heywood import reached a level that tripped the interconnector on loss of synchronism protection. The loss of power infeed from the wind farms and import from VIC resulted in the SA frequency falling so fast that load shedding schemes were unable to arrest the fall, resulting in a blackout [3, 65]. The combined inertia of the thermal generating units was around 3,000 megawatt seconds (MWs).

Fig. 4 shows a separation in the measured frequency between the two areas in the period immediately before the loss of the Heywood Interconnector. This was caused by the growing angular difference between the respective voltage phase angles, resulting in a loss of synchronism between SA and the remainder of the Australian grid.

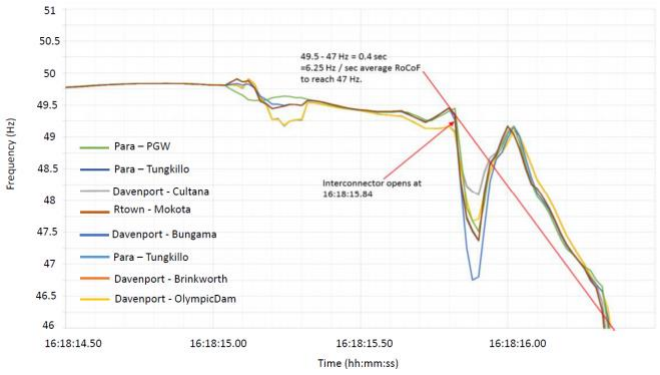

Figure 4. Frequency and its rate of change at various locations in SA. Adapted from [3].

The Australian Energy Market Operator expressed reservations about the accuracy of frequency measurements, which were probably not a true reflection of power system frequency, given the large and almost step changes in voltage phase angles in SA following separation. Those sudden angle

changes, along with the rapid changes in load due to possible operation of the UFLS scheme, have resulted in inaccuracies in short-term frequency measurements. Although the various available PMU measurements showed consistent frequency evolutions, it is not clear whether the underlying concept of phasor measurement was still applicable.

B. Event of August 25, 2018, Australia [4]

On August 25, 2018, an event saw the loss of the AC interconnector QNI between Queensland (QLD) and New South Wales (NSW) regions, followed by the loss of the AC interconnector between SA and Victoria (see Fig. 5).

The event started with a lightning strike on the double-circuit 330-kV QNI line. This triggered a series of reactions creating faults on each of the two circuits of QNI at 13:11:39. The QLD and NSW power systems then lost synchronism, islanding QLD two seconds later. At that time, 870 MW were flowing from QLD to NSW. QLD experienced an immediate supply surplus, resulting in a rise in frequency to 50.9 Hz, while NSW experienced a supply deficit, resulting in a reduction in frequency.

In response to the reduction in frequency, the SA–VIC interconnector at Heywood experienced rapid changes in power system conditions that triggered the Emergency Tripping scheme. The latter responded as designed and separated SA, which was exporting 165 MW to VIC. The corresponding surplus caused the frequency to rise in SA. At the time of the event, the loading level in SA was around 22.5 GW and 22.7 % of that power was provided by non-synchronous generators (mostly PVs).

The measured frequency signals are shown in Fig. 6. The average RoCoF, measured for data measurement durations of at least 1 s, are indicated in Fig. 7. The highest sustained RoCoF level measured in this manner during the event was around +0.65 Hz/s in SA, immediately after separation from VIC. It is worth noting that the values assumed by the RoCoF are strongly influenced by the algorithm used to measure this quantity.

Small-scale inverters interfacing PV units installed before Oct. 2015 are compliant with the standard AS 4777-2005. As a consequence, they trip if the frequency falls outside the range of operating values. Small-scale inverters installed after Oct. 2016 are compliant with the standard AS/NZ4777.2-2015 and they must not disconnect when the frequency is within the range 47-52 Hz and, as frequency rises from 50.25 Hz toward 52 Hz, they should reduce their output linearly from the pre-disturbance output at 50.25 Hz, reaching zero at 52 Hz [66]. Moreover, active power output should be held at the lowest until frequency has returned to the range 49.85-50.15 Hz. Units installed meanwhile may be compliant with either standard.

In areas undergoing over-frequency, a combination of disconnections and power output reductions led to a net increase of the load helping to mitigate the frequency rise. In areas undergoing under-frequency, only disconnection of some "old" inverters was observed. Yet, a small fraction of inverters compliant with the new requirements disconnected while they should have remained in operation.

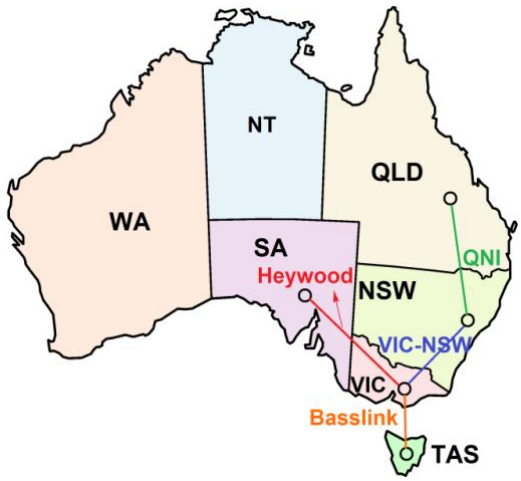

Figure 5. Affected transmission links during the event of August 25, 2018 in Australia.

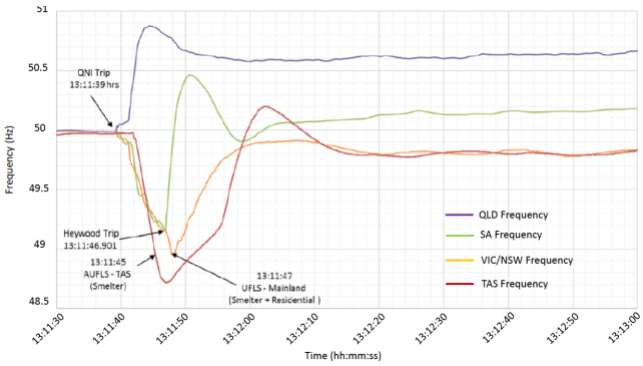

Figure 6. Measured frequency signals. Adapted from [4].

As regards transmission-connected PV plants, they should respond to over-frequency by reducing their active power output with a droop value between 2 and 10 %, and holding the lowest output until frequency returns to acceptable values. No under-frequency response is required.

Therefore, in QLD and SA, where frequency rose, the output of PV plants decreased while no noticeable variations were observed in other regions. In QLD, most of the reduction in generation was observed after peak frequency was reached. Some inverters even started to trip as frequency remained above 50.5 Hz for more than 10 minutes. In SA, the single PV plant in operation was not able to control the frequency overshoot following the Heywood trip, due to a large delay of about 4 s from frequency measurement to plant reaction.

SA has two transmission-connected battery systems. Only one, with a capacity of +100 MW/-80 MW, was in operation, charging at -38 MW prior to the event. This battery has a proportional power response to frequency deviations (100 MW/Hz). Its rapid response helped limiting the frequency excursions. However, its response to the initial under-frequency contributed to the tripping of the interconnector by increasing

the power transfer from SA towards VIC. Since then, the tripping scheme has been revised.

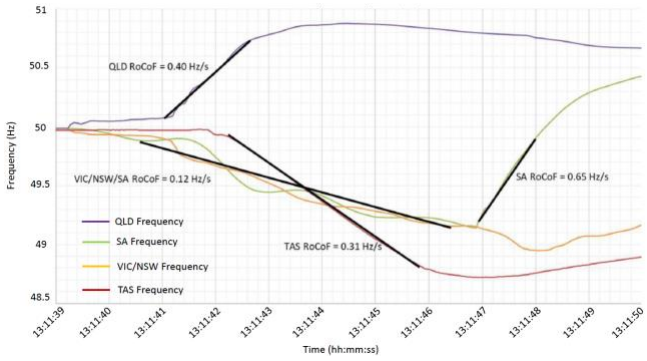

Figure 7. Regional Frequencies and RoCoFs during the event. Adapted from [4].

C. *Event of August 16, 2016, California, USA*

On August 16, 2016, a fault induced a total of 1,178 MW of PV power interruption. The faults were caused by a fire that started at the Cajon Pass in California, USA and moved towards a major transmission corridor with three 500-kV lines and two 287-kV lines. There were multiple faults over a period of time: thirteen on the 500-kV system and two on the 287-kV system. The fault that induced the loss of 1,178 MW occurred at 11:45am and was successfully cleared in less than three cycles. As a result of the fault, the solar PV plant inverters ceased output. Specifically: (a) the majority of inverters trip instantaneously based on frequency measurements obtained from PLLs; it was determined that these inverters are susceptible to erroneous tripping due to frequency changes; this response accounted for 700 MW of the lost generation; and (b) a number of inverters that tripped were configured to cease current injection if the voltage goes above 1.1 pu or below 0.9 pu; the inverters were returned to pre-disturbance level at a slow ramp rate; this response accounted for about 450 MW of lost generation. Approximately 66% of lost generation were restored within five minutes.

The frequency during the above described event is shown in Fig. 8 and the waveform distortion is shown in Fig. 9. These figures provide evidence of the response of the inverters. The phase shift observed in the waveforms generates a large instantaneous frequency change in most frequency tracking algorithms and in this case triggered the inverters responses. Note that the frequency evolution in Fig. 8 does not show the spikes since it was obtained with PMUs that show average frequency over longer windows. Note also that the voltage during the fault dropped below 0.6 pu triggering the ride-through function which in this case did not return to the pre-disturbance values fast enough.

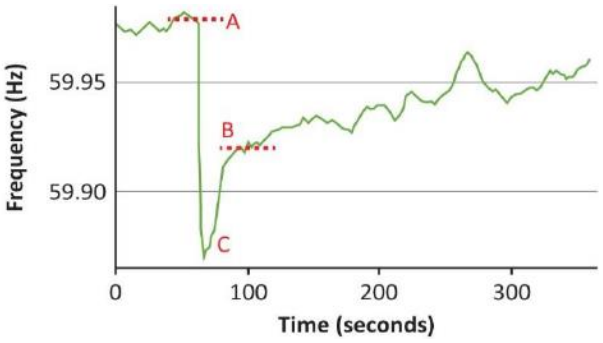

Figure 8. Western Interconnection Frequency During the 11:45am PST Fault [67].

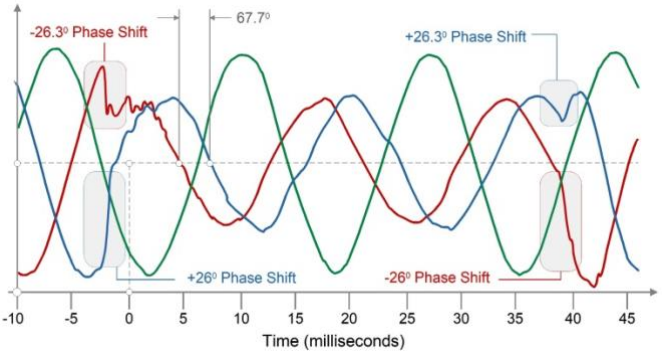

Figure 9. Distortion of Sine Waves During the 11:45am PST Fault [67].

D. *Event of October 9, 2017, California, USA*

On October 9, 2017, a fire in California (Canyon 2 fire) caused two transmission line faults 2 minutes and 14 seconds apart on a 220-kV and a 500-kV transmission line, respectively. The faults were successfully cleared but the disturbance caused the loss of 900 MW of solar PV resources in about six PV plants [68]. The majority of inverters trippings was caused by fast transient overvoltages (sub-cycle) and instantaneous protecting actions. A significant number of inverters entered momentary cessation following the fault events. Note that, in this case, no instantaneous tripping occurred due to instantaneous fast frequency changes; the instantaneous tripping was due to transients. The activation of the ride-through function was also a contributing factor as the return to pre-disturbance operation was characterized by a long delay and a slow ramping.

E. *Lessons from these examples*

Both California events were caused by inverter controls and, more specifically, protection settings including instantaneous frequency/transients and ride-through function settings. These cases provide useful information for better design of inverter controls. Although some of the incidents resulted from severe system splits, the above examples of large frequency excursions foreshadow situations likely to occur more frequently and, in more systems, owing to the decreasing kinetic energy storage in synchronous machines. All four examples illustrate the need for better signal processing

techniques to extract relevant information in the presence of rapid frequency changes and/or transiently distorted sinusoidal waves. Otherwise it is likely that the security and dependability of protections fitted to the inverters will worsen, causing trippings that aggravate the severity of the initiating fault. In parallel, attention must also be paid to modelling both legacy and recent (or future) protections of converters in order to account for their response to faults. The same applies to their controls, as stressed by the examples of slow recovery of the active power of converters that have ridden through faults.

IV. ADEQUACY OF SIGNAL PROCESSING TECHNIQUES

A. Phasor representation limits

Recent studies (e.g. [69]) discussed the limitations of the time-scale separation associated to the use of a quasi-stationary power grid models relying on phasors when the grid hosts large amount of CIG. In this respect, this section provides a detailed analysis of these limitations.

1) Models of power systems signals

Time-domain steady-state sinusoidal signals (i.e., with amplitude A_0 and frequency f_0 that do not vary with time) associated with power systems voltages and currents represented as in (2), can be mapped by means of a bijective transformation onto complex quantities called *phasors*. This refers to the FT and it is usually realized by means of the discrete Fourier transform (DFT) applied on a finite time window T of $x(t), t \in [t_0, t_0 + T]$ (e.g. [70]).

$$x(t) = A_0 cos(2\pi f_0 t + \varphi_0) \overset{DFT}{\Longleftrightarrow} X = A_0 e^{j\varphi_0} \quad (2)$$

In (2) we supposed the time window T to contain an integer number of periods $1/f_0$. However, in power systems voltage or current signals are rarely in steady-state, since they are characterized by time-varying parameters associated with broad- and/or narrow-band transient disturbances and/or permanent components. A more generic model of the signal $x(t)$ is the one given by (3) and adapted from [71]:

$$x(t) = A_0(t)\left(1 + \varepsilon_{A_0}(t)\right) cos\left(2\pi f_0(t)t + \varphi_0 + \varepsilon_{\varphi_0}(t)\right) + \eta(t) + \\ + \gamma(t) + \nu(t) \quad (3)$$

where:

- the fundamental component amplitude $A_0(t)$ and frequency $f_0(t)$ are varying with respect to time.
- $\varepsilon_{A_0}(t)$ represents the fundamental component amplitude fluctuations (e.g., amplitude modulations).
- $\varepsilon_{\varphi_0}(t)$ accounts for the presence of phase modulations;
- $\eta(t)$ models narrow-band disturbances like harmonics and/or inter-harmonics. Therefore, it can be expressed as $\eta(t) = \sum_h A_h(t)\left(1 + \varepsilon_{A_h}(t)\right) cos\left(2\pi f_h(t)t + \varphi_h + \varepsilon_{\varphi_h}(t)\right)$ being $h = f_h/f_0$ the harmonic and/or inter-harmonic component order, $A_h(t)$ is the harmonic and/or inter-harmonic component amplitude with initial phase φ_h where time-varying quantities $\varepsilon_{A_h}(t)$ and $\varepsilon_{\varphi_h}(t)$ model any amplitude and phase/frequency fluctuations of these last components.
- The term $\gamma(t)$ in (3) may represent DC decaying components while $\nu(t)$ accounts for the so-called grid noise (for example, thermal, corona, partial discharges).

It is worth observing that the signal model (3) significantly differs from (2) as well as from the definition of phasors provided by the IEC/IEEE Std. 60255-118-1 [72]. Indeed, this standard has tried to solve the above discrepancy by introducing the following signal model.

$$x(t) = A_0(t) cos(2\pi f_0(t)t + \varphi_0) \overset{DFT}{\Longleftrightarrow} X(t) = A_0(t) e^{j\Phi_0(t)} \quad (4)$$

Since in (4) the instantaneous phase $\Phi_0(t)$ takes into account both the frequency and initial phase, setting a constant initial phase implies that instantaneous phase variations are only due to the power system frequency variations avoiding the possibility of having multiple couples of frequency and initial phase producing the same instantaneous phase $\Phi_0(t)$. The same observation holds also for (3). Although the signal model (4) accounts for time-varying amplitude and frequency of the fundamental component of power systems signals, it still significantly differs from the model (3). Indeed, the model (4) works pretty well when the DFT spectrum of the signal can be approximated by a finite set of bins given by the fundamental component and the harmonic ones [73]. In the presence of large power systems dynamics (including those associated to lack of system inertia) the model in (4) is still not entirely appropriate as it cannot account for rapid variations of signal parameters with a satisfying level of accuracy.

2) Spectrum of signals characterised by high RoCoF

Regarding signal dynamics with respect to frequency variations, reduced inertia systems may experience RoCoF values of several Hz/s (high RoCoF can be also seen locally in a low inertia area connected to a high inertia area where a large disturbance is taking place). An example of this type of dynamics was experienced during the South Australian system blackout that took place on September 2016 (see section III.A for further details). Fig. 10 shows the frequency recorded by phasor measurement units (PMUs) installed in that area during the whole event. The frequency experienced a complex dynamic with a maximum RoCoF in the order of 10 Hz/s with an average weighted ROCOF of -6.25 Hz/s within the time interval from *t*=3.7 and *t*=3.9s (see also Fig. 4). Let us synthesize and analyse a broad-band signal (e.g., a node voltage) that, starting from a steady state frequency $f_0 = 50Hz$, experiences a decreasing frequency ramp $R = -6.25Hz/s$, namely $v(t) = A_0 cos(2\pi(f_0 - Rt)t)$ (we assume $A_0 = 1$). Fig. 11 shows the spectrum of $v(t)$ computed by means of a DFT applied over a window of 1 s, leading to a spectrum granularity of 1 Hz. It is worth observing that the broad-band spectrum of this signal does not extend beyond 100 Hz. Therefore, the sampling frequency of the signal does not affect the results shown in Fig. 11 as long as it does not produce any aliasing effect (for this specific simulation, we adopted a sampling frequency of 10 kHz). Fig. 11 shows that only 32% of

the signal energy[1] is within the range between 48 and 52 Hz while the rest of the signal energy is spread in a continuous spectrum extending well beyond the fundamental component. In other words, we are in the presence of a broad-band signal that cannot modelled by means of a phasor at a fixed frequency. This preliminary analysis is further developed in the next section.

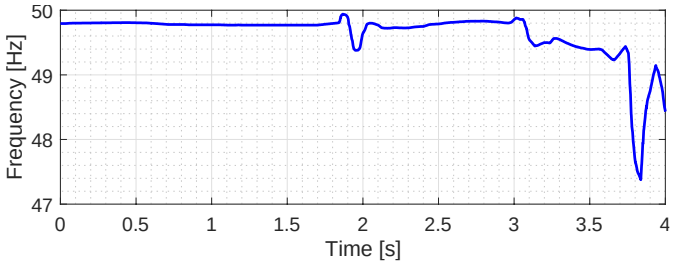

Figure 10. Frequency estimated by PMUs during the South Australian blackout on September 2016.

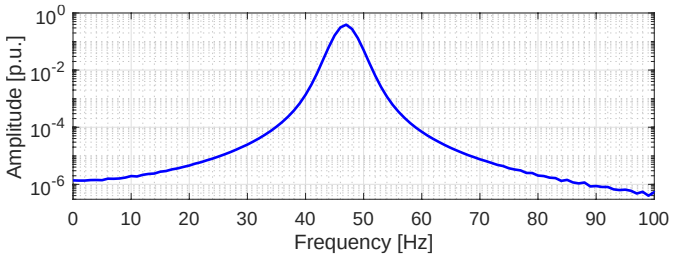

Figure 11. Normalised spectrum of a signal characterised by a ROCOF of -6.25 Hz/s computed by means of a DFT applied over a window of 1 s. Adapted from [26].

B. Phasor analysis in the presence of broad-band signals

The previous section has discussed the adequacy of the phasor model to represent broad-band signals. This section extends the development by discussing the appropriateness of phasor representation to compute the instantaneous electric power in the presence of broad-band signals. In particular, we use a DFT-based technique to estimate the instantaneous power transfer during severe electromechanical transients and this application makes use of the IEC Std. 61000-4-7 [74] as it is one of the most updated guide on harmonics and interharmonics measurements for power supply systems. More specifically, the investigation focuses on the estimation of the instantaneous[2] three-phase power transfer in the presence of a broad signal spectrum using a simple 2-bus system shown in Fig. 12. For this analysis, we perform dedicated off-line simulation using the EMTP-RV [75]. The simulations refer to the simple model shown in Fig. 12 consisting of a time-varying 3-phase voltage generator supplying a 400 MW load through an overhead transmission line. The voltage source can generate any generic waveform and is characterized by a nominal voltage of 380 kV (phase-to-phase) at 50 Hz. We consider a 100 km aluminium conductors steel reinforced overhead line modelled using a standard ∏-circuit line model. The load, instead, is modelled by means of a constant impedance tuned to absorb a rated power of 400 MW with a 0.9 (lag) power factor when supplied in nominal conditions (i.e., with a sinusoidal voltage at 50 Hz and 380 kV). We set the voltage at the generator and the load impedance and we analyse the corresponding voltage and current signals supplying the load (i.e., node B in Fig. 12).

The proposed phasor-based analysis is inspired by the IEC Std. 61000-4-7 [74]: by means of sliding windows of 200 ms, the observation interval is shifted sample-by-sample and, for each window, the FT is approximated by means of the DFT. The adopted window length determines a 5 Hz resolution of the frequency spectrum that may lead to spectral leakage and low spectrum granularity. In order to mitigate these detrimental effects, the signal is windowed with the Hanning weighting function and the fundamental component parameters are determined by means of the so-called enhanced interpolated-DFT [76]. Amplitude, frequency and phase estimates are used to approximate the time domain trend of the sinusoidal component in the considered observation interval.

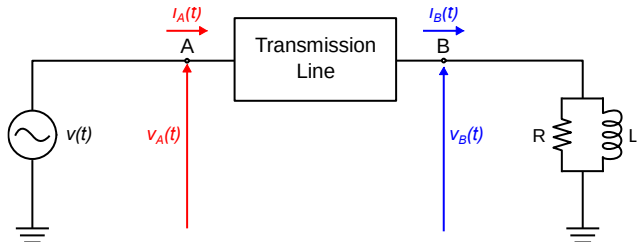

Figure 12. Block diagram of the adopted EMTP-RV simulation model. The generator is characterized by nominal (phase-to-phase) voltage of 380 kV, and is connected to a 400 MW load through a 100 km overhead line.

In this controlled experiment, we synthesize dynamic voltage waveforms that are applied to the system by the voltage source at node *A* of the two-node system shown in Fig. 12. In particular, we consider two cases: (i) a negative frequency ramp characterized by RoCoF of -5 Hz/s and (ii) an amplitude modulation characterized by 10% depth and 5 Hz modulating frequency. Reference [26] provides a similar analysis for other dynamic operating conditions and the reader can refer to this paper to see the broad applicability of the process here described. We simulate a plausible measurement system where the voltage and current waveforms are sampled at 10 kHz. The DFT-based analysis is applied to the voltage and current signals measured at node *B* (see Fig. 12). The obtained phasors are used to estimate the load three-phase instantaneous power and the associated error. In particular, the power error is calculated as the difference between the instantaneous power obtained from the time-domain voltage and current waveforms coming from the simulation and the instantaneous power obtained from reconstructed time-domain voltage and current waveforms

[1] We remind that the energy of a signal $x(t)$ is defined as $\int_{-\infty}^{-\infty}(x(t))^2\,dt$ although, for time-limited signals like windowed ones, it is computed as $\int_{t_1}^{t_2}(x(t))^2\,dt$ being t_1, t_2 the bounds of the signal time window.

[2] The use of the instantaneous power is justified in order to avoid the non-unique interpretation of active and reactive powers associated with the use of a steady-state phasor representation of currents and voltages (see also section II.D).

obtained after the use of the interpolated DFT to estimate the fundamental frequency component of the signals under analysis. Figs. 13 and 14 show the results of the proposed analysis. In particular, the top graphs show the true voltage waveforms as provided by the EMTP simulations and the signals reconstructed using the phasor-based analysis. The middle graphs represent the resulting three-phase instantaneous power delivered to node *B* computed as the product between the time-domain voltage and current signals (true vs phasor-reconstructed). The bottom graphs show the corresponding three-phase power errors, computed as the difference between the phasor-reconstructed instantaneous three phase power and the true one.

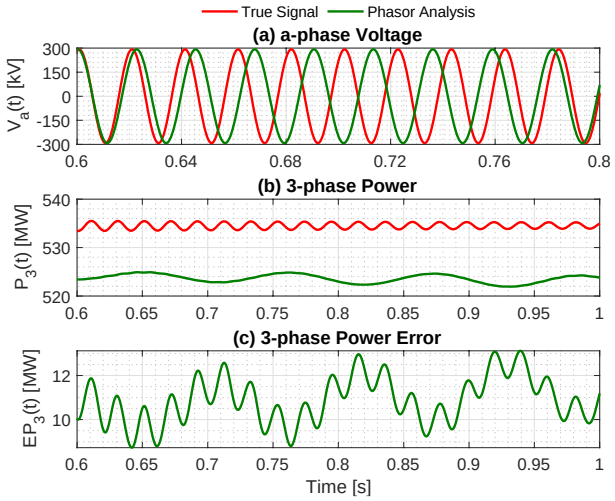

Figure 13. Analysis of two-bus system of Fig. 12 when the supplying voltage at node *A* experiences a negative frequency ramp of -5 Hz/s: a) true (simulated) and phasor-reconstructed phase-to-ground voltage waveforms, b) true and phasor-reconstructed instantaneous three phase power, c) error of the phasor-reconstructed three phase power.

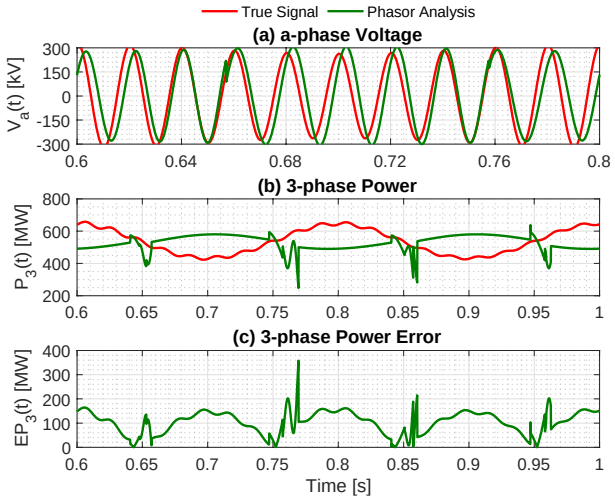

Figure 14. Analysis of two-bus system of Fig. 12 when the supplying voltage at node *A* experiences a 10% amplitude modulation with modulating frequency of 5 Hz: a) true (simulated) and phasor-reconstructed single-phase voltage waveforms, b) true and phasor-reconstructed instantaneous three phase power, c) error of the phasor-reconstructed three phase power.

Regarding the frequency ramp, Fig. 13 shows that, as the frequency deviates from its nominal value, the phasor analysis provides erroneous results due to spectral leakage. Furthermore, the true waveform experiences a frequency variation that is evident also in half a cycle that cannot be followed by a phasor reconstruction of the same signal. The consequence is that the maximum obtained power errors are in the order of 13 MW (i.e. 2.5% of the total power transfer). With regards to the amplitude modulation, Fig. 14 shows that the phasor representation does not enable to correctly interpret a signal whose fundamental component is modulated. Indeed, the obtained signal spectrum is largely biased by the interference produced by the modulating term, leading to imprecise and shifted in phase parameters estimation. Both voltage and current are inaccurately reconstructed, leading to a maximum power error above 200 MW (i.e., 40% of the total power transfer).

C. Analysis of broad-band signals using the Hilbert Transform

Given the limitations associated with a single-component phasor-based representation, this section summarizes a different approach for modelling broad-band signals that goes beyond the concept of static phasor based on the FT. The study is inspired by the theory on analytic signals and is based on the Hilbert transform (HT). More specifically, the method has been proposed in [26] and estimates the parameters of a generic signal under test by means of functional analysis [27].

We first recall the theoretical foundations of the method. Then, we describe the process to estimate the parameters of the functional basis. Finally, the performance of the proposed method is assessed by means of a dedicated time-domain simulation replicating a signal characterized by a negative RoCoF of -5 Hz/s (as in Section IV.A).

Among the possible electromechanical transients, in this section we investigate the case of a power system signal, say a nodal voltage, whose frequency is decaying with a descending ramp trend. This is typical of the stages anticipating a severe system collapse like the one that took place in South Australia on September 2016 (see Figs. 4 and 10). As discussed in [26], a similar approach can be extended to the analysis of other power system transients, such as amplitude, phase and frequency modulations or steps.

For the sake of nomenclature, we recall the fundamentals of the HT. For a generic time-varying signal $x(t)$, its HT $\mathcal{H}[\cdot]$ is defined as [77]:

$$\tilde{x}(t) = \mathcal{H}[x(t)] = \frac{1}{\pi}\int_{-\infty}^{+\infty}\frac{x(\tau)}{t-\tau}d\tau \tag{5}$$

The combination of the real signal $x(t)$ and its HT $\tilde{x}(t)$ form the so-called *analytic signal* $\hat{x}(t)$:

$$\hat{x}(t) = x(t) + j\tilde{x}(t) \tag{6}$$

It is worth recalling that in signal processing the analytic signal defined by (6) allows to obtain a complex-valued function that has no negative frequency components in its spectrum.

By making reference to (3), a generic frequency ramp can be modelled as a function of the ramp rate R as:

$$x(t) = A_0\, cos(2\pi f_0 t + \varphi_0 + 2R\pi t^2) \quad (7)$$

The FT of such signal is reported in (8) and it does not allow to distinguish the fundamental component from the spurious contributions introduced by the time-varying frequency:

$$\mathcal{F}[x(t)] = \frac{A}{2\sqrt{2}} e^{j\left[\frac{\pi(f-f_0)^2}{R} - \frac{\pi}{4} + \varphi_0\right]} + \frac{A}{2\sqrt{2}} e^{-j\left[\frac{\pi(f+f_0)^2}{R} - \frac{\pi}{4} + \varphi_0\right]} \quad (8)$$

On the other hand, the HT provides the analytic signal (9) that can be regarded as a dynamic phasor characterized by constant amplitude and rotating as the frequency ramp.

$$\hat{x}(t) = A_0 e^{j(2\pi f_0 t + \varphi_0 + R\pi t^2)} \quad (9)$$

Note that (9) has been derived assuming that the HT of the product of two signals with non-overlapping spectra is equal to the product of the low-frequency term and the HT of the high-frequency term [26].

It is worth pointing out that the analytic signal in (9) is a closed-form expression of the real-valued signal in (7). In other words, the HT may provide an exact match between the real-valued time-domain signal and its analytic representation. Therefore, if we project the real-valued signal in (7) over a basis containing the analytic signal in (9), we would obtain a projection coefficient that unequivocally identifies the parameters of the signal in (7). By generalizing this reasoning to other non-stationary signals, it is possible to build a *suitable dictionary that contains several of the so-called atoms, each representing a specific function*. If we project any generic time-domain signal $x(t)$ over such a functional basis, in principle, we would be able to obtain the mathematical formulation of any signal under investigation $x(t)$.

Based on this idea, in the method proposed in [26] we define the analytic signals of several dynamics that are likely to take place in the power system context and we construct a dictionary D that contains their frequency-domain representations. In particular, the analytic atoms, i.e., the lines of the dictionary, are formulated as follows:

$$d = DFT[(1 + g_A(t)) \cdot e^{j(2\pi g_f(t)t + g_\varphi(t))}] \quad (10)$$

The functions g_A, g_f and g_φ account for the time-variations of amplitude, frequency and phase of the fundamental component. It is worth pointing out that the use of analytic signals enables us to define atoms that are not pure sinusoidal components as they consist of modulated complex exponentials that better match the broad-band spectrum of the dynamics under investigation.

The projection of the generic signal over the basis D enables the identification of a mathematical model of the parameters' evolution that, de facto, enables the compression of the time domain information into few coefficients of (10). The performance of the projection depends on the number of possible realizations of (10) included in the basis although may become computationally demanding and numerically ill-conditioned due to the high correlation between the elements of the basis.

As an example, a set of disturbances inspired by [72] that are likely to take place in power systems are taken into account to build the dictionary D. More specifically, the frequency of the fundamental component is limited to a finite bandwidth between 48 and 52 Hz with steps of 0.01 Hz and, for each fundamental frequency, the following vectors are included in D (note that the modeler is free to restrict the dictionary to the components he considers to be relevant):

- A steady-state sinusoid (g_A = 0, dg_f/dt = 0, g_φ = 0);
- A sinusoid characterized by an amplitude modulation $g_A(t) = 1 + k_a \cos(2\pi f_a t)$, being k_a = 10% and f_a = [1,5] Hz with steps of 0.01 Hz (dg_f/dt = 0, g_φ = 0);
- A sinusoid characterized by a frequency ramp $g_\varphi(t) = R\pi t^2$, being R = [-7, 7] Hz/s with steps of 0.01 Hz/s (g_A = 0, dg_f/dt = 0);
- A sinusoid characterized by an amplitude step $g_A = k_s h_s(t - \tau)$, being k_s = 10% and τ = [0, 200] ms with steps of 5 ms (dg_f/dt = 0, g_φ = 0).

The functional analysis is implemented via the Algorithm #1 and further details can be found in [26] and described next. Starting from the sampled signal $x(t)$, the user should be able to define its HT, $\mathcal{H}[x(t)]$, in order to build the analytic signal $\hat{x}(t)$. The analytic signal of the waveform under test is here computed by means of a complex filter H that approximates the ideal HT (line 1 of Alg#1). Then, the spectrum of the analytic signal, $\hat{X}$, is determined by means of a standard DFT (it is worth noting that this spectrum does not contain its negative image thanks to the properties of $\hat{x}(t)$) (line 2 of Alg#1). Here, the DFT of the analytic signal is computed over overlapping windows of 200 ms. The DFT-spectrum is projected onto the dictionary D in order to determine the projection vector P, being $D^\dagger$ the Hermitian transpose of D (line 3 of Alg#1). The projection errors are defined as the difference between the spectrum reconstructed for each dictionary element and the actual analytic spectrum $\hat{X}$. The residuals relative to these errors are computed (line 4 of Alg#1) and the vector of D, alogn with the relevant projection coefficients, minimizing the residuals are identified as the most representative of the signal components with respect to the dictionary D (line 5 of Alg#1). The product of D with the corresponding projection coefficient n_{coef} gives the best estimate of the signal $\hat{x}_\mathcal{H}(t)$ (line 6 of Alg#1). The module of difference between the original signal and the $\hat{x}_\mathcal{H}(t)$ is the most relevant error metric quantifying the difference between the original signal and its best estimate.

Algorithm #1: Functional basis analysis of generic signals

1: $\hat{x}(t) = x(t) + j\mathcal{H}[x(t)] \approx H[x(t)]$
2: $\hat{X} = DFT[\hat{x}(t)]$
3: $P = D^\dagger \hat{X}$
4: $N = norm[D^\dagger \hat{X} D - \hat{X}]$
5: $[n_{idx}, n_{coef}] = min[N]$
6: $\hat{x}_\mathcal{H}(t) = n_{coef} \cdot D(:, n_{idx})$
7: $x_E(t) = |\hat{x}_\mathcal{H}(t) - x(t)|$

In order to assess the performance of such an approach, we analyse signals that represent voltage and current waveforms by making reference to the model in Fig. 12. As for the simulations carried out in section IV.A, we set the time-domain voltage waveform at the voltage source in node *A* and we use Algorithm #1 to estimate the parameters of the resulting voltage and current signals at node *B*, as well as the associated three-phase power. Then, we estimate the same signals' parameters with the method based on the interpolated DFT adopted in section IV.A.

Fig. 15 shows the results in case the generator outputs a voltage signal as in (7) with a frequency ramp rate of -5 Hz/s. As already seen in section IV.A, as the frequency deviates from its nominal value, the DFT cannot exactly reconstruct the voltage and current signals due to spectral leakage, leading to power errors in the order of 12 MW. Conversely, the functional analysis based on the HT is able to follow instantaneously the signal dynamics experienced during a frequency ramp, providing an almost-perfect signal and power flow reconstruction, characterized by errors lower than 10 kW.

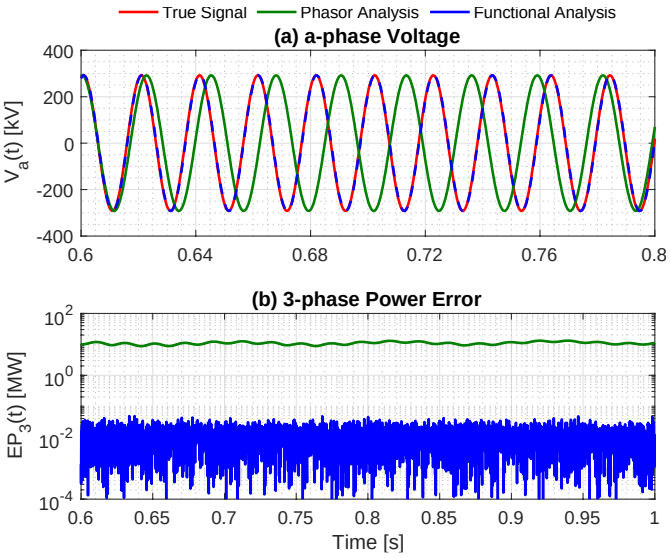

Figure 15. Analysis of two-bus system of Fig. 12 when the supplying voltage at node *A* experiences a negative frequency ramp of -5 Hz/s: a) true (simulated), phasor-reconstructed and functional-analysis reconstructed phase-to-ground voltage waveforms, b) true, phasor and functional-analysis reconstructed instantaneous three phase power, c) error of the phasor and function analysis reconstructed three phase power.

D. Base-band representation for modelling and simulation

The common denominator of the signal analysis methods described in previous paragraphs is the idea to substitute the signal with a base-band representation in terms of a complex number. First examples of this approach are reported as dynamic phasor approaches and they are based on the idea of representing a signal by means of a frequency shifted complex representation [78-80]. One way to obtain such a description, is to shift the analytic representation $x_a(t)$ of a real signal $x(t)$ by an arbitrary frequency ω_c. Assuming that the real signal is exactly described by the analytic signal $x_a(t) = A(t)\, e^{j\theta(t)}$, the frequency shift by ω_c can be expressed as follows:

$$x_a(t) = A(t)\, e^{j\theta(t)-j\omega_c t+j\omega_c t} = \\ = A(t)\, e^{j\varphi(t)}\, e^{j\omega_c t} = \langle x_a \rangle(t)\, e^{j\omega_c t} \tag{11}$$

where $\langle x_a \rangle(t) = x_a(t)\, e^{-j\omega_c t}$ is shifted in frequency with respect to $x_a(t)$ and $\varphi(t) = \theta(t) - \omega_c t$.

$\langle x_a \rangle(t)$ is a frequency shifted complex representation, which can be used in the numerical simulation of dynamical models. To calculate the derivative of such a variable as it is often required in dynamical models, the chain rule can be applied:

$$\frac{d}{dt}\langle x_a \rangle(t) = \frac{d}{dt}\left(A(t)\, e^{j\varphi(t)}\right) \\ = \frac{d}{dt}\left(A(t)\, e^{j\theta(t)-j\omega_c t}\right) \\ = \frac{d}{dt}\left(A(t)\, e^{j\theta(t)}\right)e^{-j\omega_c t} + \left(A(t)\, e^{j\theta(t)}\right)\frac{d}{dt}e^{-j\omega_c t} \\ = \frac{d}{dt}\left(A(t)\, e^{j\theta(t)}\right)e^{-j\omega_c t} - j\omega_c\left(A(t)\, e^{j\theta(t)}\right)e^{-j\omega_c t} \\ = \left(\frac{d}{dt}x_a(t)\right)\, e^{-j\omega_c t} - j\omega_c\, x_a(t)\, e^{-j\omega_c t} \tag{12}$$

Following the same logic as before, this can be rewritten as:

$$\frac{d}{dt}\langle x_a \rangle(t) = \langle \frac{d}{dt}x_a(t) \rangle \; - j\omega_c \langle x_a \rangle(t) \tag{13}$$

Therefore, the exact derivative of the simulation variable $\langle x_a \rangle(t)$ can be calculated if the analytical representation $x_a(t)$ and its derivative are available. In case $x_a(t)$ is approximated, also the simulation variable $\langle x_a \rangle(t)$, its derivative and eventually the dynamical model is an approximation.

The frequency shifted complex representation $\langle x_a \rangle(t)$ is commonly denoted as baseband representation or complex envelope. The baseband representation holds all the information about the original signal except for the center frequency ω_c and it is complex valued like the phasors used in quasi-stationary electrical simulations. The difference is that the models based on this representation and the approach described before do not neglect dynamics, which is why it is commonly referred to as dynamic phasor.

If the real signal is measured and it is not given in mathematical terms, there exist several approaches to extract a complex valued approximation. Two of these are Fourier and Hilbert transforms.

The Fourier approach is well suited for multi-component signals that feature several narrow band bins in the frequency domain. Each of these bins is mapped to one complex phasor. This approach comes mostly from the power electronics area thanks to the concept of generalized state space averaging. In this approach, the complex phasor is approximated by a Fourier coefficient that is dynamically changing with time. A key role is played by the observation window T. In formulae:

$$\langle x \rangle_k(t) = \frac{1}{T}\int_{t-T}^{T} x(\tau)\cdot e^{-jk\omega_c \tau}\, d\tau \tag{14}$$

A signal can then be approximated by a set of complex numbers each one corresponding to a different central frequency or bin, which is advantageous whenever we deal with signals with significant distortion.

The HT, as described earlier, is the natural choice if the complex representation of a single-component narrowband is required. Often, it is applied in combination with mode decomposition, which makes it possible to process each mode separately. The combination of Hilbert and mode decomposition is widely known as Hilbert-Huang transform [81]. The difficulty of the Hilbert-Huang transform is that it is empirical and not analytically defined as the Hilbert and Fourier transform.

In any case, whatever approach is used for the formulation, the base-band representation offers a very powerful modelling framework that performs an optimization of the time step selection whenever we perform simulation at run time. As a result of the definition of the derivative operator explained earlier, an easy translation of a model in the classical time-domain to the base-band domain can be performed determining a new set of models that can be adopted for large system simulation.

Models defined in this domain can also be combined using classical simulation methods, such as nodal analysis, to create an open solver able to fully exploit the flexibility of this representation. The main element of flexibility is the fact that a model defined in this domain has the capability to serve different level of details without reformulating the equations.

Let us suppose now to use such an approach to develop a time-domain simulator. A key feature of this kind of simulator is the role played by the time step compared with classical solvers. The time-step serves as an automatic adapter for the model that can span from quasi-stationary to classical EMT analysis [82]. The concept can be exemplified with reference to a simple linear capacitor model described with a resistive companion approach [83]. Each simulation step of the capacitor model in the new domain is represented by the following equation (see also Fig. 16):

$$\langle i_C \rangle(k) = \frac{1+jb}{a} \langle v_C \rangle(k) + \langle i_{C,equiv} \rangle(k-1) \qquad (15)$$

where: $a = \Delta t/2C$, $b = \Delta t\omega/2$ and $\langle i_{C,equiv} \rangle(k-1) = \frac{1+jb}{a} \langle v_C \rangle(k-1) + \langle i_C \rangle(k-1)$.

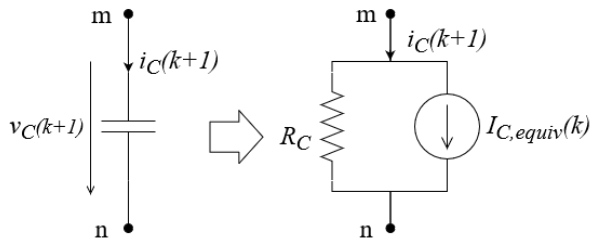

Figure 16. Discrete-time resistive companion representation of a capacitor.

It is interesting to make note the following.

- When the time step grows indefinitely the model tends to disregard the dynamic component and becomes a standard steady state phasor.
- When the time step tends towards a very small value, the model converges to the classical representation of a capacitor in resistive companion adopted for EMT simulation.

Whenever the models are linear, the discrete time representation in the resistive companion circuit is numerically stable, while the selection of the time steps affects only the accuracy of the results. In this process, the model changes automatically as a function of the time step depending on the level of dynamics we want to track in the simulation.

As result, for slowly changing dynamics, the time steps can be chosen to be significantly large (for a classical grid in the range of several millisecond); while during fast transients the time step can be reduced to keep the accuracy under control. The value of this approach can be proved with the support of some examples [84,85].

Let us consider first the CIGRE MV benchmark grid with high penetration of PV sources [86] and let us apply a change of load power at the end of the feeder from 100% to 150% of the nominal value. Such a transient determines significant oscillation in the feeder current as reported in Fig. 17. It is interesting to observe that the base-band solvers (in the figure indicated with DP) executed with 100 μs time step presents results very similar to a classical EMT simulation with resistive companion executed at 50 μs. Vice versa, using a classical static phasor representation the accuracy is compromised.

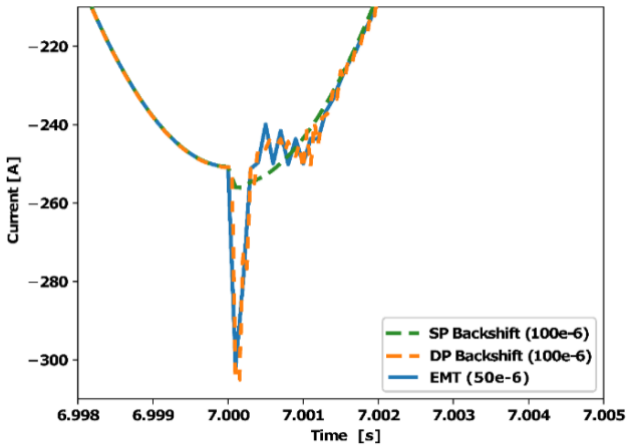

Figure 17. Feeder current during load transient (comparison of three simulation approaches).

Other interesting results are reported in Figs. 18 and 19 showing the simulation of a simple resistive inductive circuit fed with a sinusoidal source at 60 Hz. The central frequency is still selected at 50 Hz. With a time-step of 100 μs, both EMT and DP present very accurate results. Once the time step is increased to 10 ms only the DP preserves the accuracy showing

how dynamically the time step can be executed and then supporting the simulation of large systems with a reasonable computational effort. By applying multiple central frequencies, it is possible also to perform detailed dynamic analysis of systems in the presence of power electronics switching at relatively high frequency (kHz range).

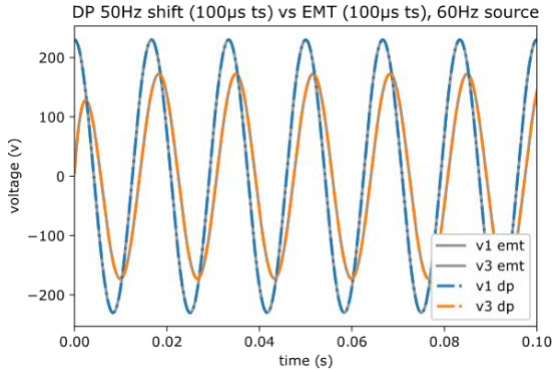

Figure 18. Voltage across the inductor with source at 60 Hz, time step at 100 μs and central frequency at 50 Hz.

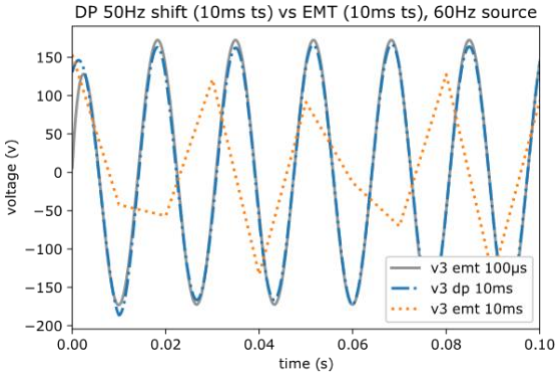

Figure 19. Voltage across the inductor with source at 60 Hz, time step at 10 ms and central frequency at 50 Hz.

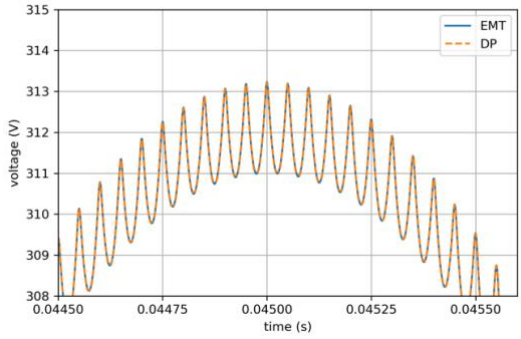

Figure 20. Simulation of a single-phase inverter switching at 10 kHz. Voltage measured at output of an LC filter.

Results in Fig. 20 are obtained by using 8 central frequencies. The DP simulation is still faster thanks to an increased time step and the exploitation of a very large sparse matrix describing the model. Sparsity effects also increase with the size of the model.

E. *Analysis of Park's transform in the presence of broad-band signals*

The Park's transform forms the basis for the reference frame representation of three-phase AC systems. It originates from, but is not limited to, synchronous machine theory and it consists of the following time-dependent transformation from the *abc* phase quantities to the *dqo* reference frame currents/voltages:

$$i_{dqo} = K\, i_{abc} \qquad v_{dqo} = K\, v_{abc} \tag{16}$$

where the 3x3 transformation matrix is defined as:

$$K = \frac{2}{3}\begin{bmatrix} \sin\theta & \sin(\theta - 2\pi/3) & \sin(\theta + 2\pi/3) \\ \cos\theta & \cos(\theta - 2\pi/3) & \cos(\theta + 2\pi/3) \\ 1/2 & 1/2 & 1/2 \end{bmatrix} \tag{17}$$

and $\theta(t) = \omega t$.

Choosing ω to be the system base electrical frequency in radians per second ($\omega_b = 2\pi f$) the *dq* frame is rotating at this constant speed and the *d*- and *q*-axis projections form the real and imaginary parts of a phasor in the base system frequency. The zero-axis component (i.e., the homopolar one) corresponds to the zero sequence of the classical positive, negative and zero sequence circuit representation.

If the three-phase system is balanced and in sinusoidal steady state, the phasor will be constant in the *dq* frame if the frequency is equal to ω_b. Otherwise, the phasor in the *dq* frame will be a rotating one at the slip frequency $\omega_b - \omega$. In the presence of negative sequence component, the phasor will consist of a constant part and a component rotating at double the synchronous speed in the *dq* frame. If a DC, or a second harmonic is present in the *abc* system, a component rotating at synchronous speed will appear in the *dq* frame.

Reference frame theory is a powerful tool to represent time varying phasors. However, the user has to keep in mind that circuit equations are not purely algebraic equations, but include also the time derivative of current/voltage components associated to the time-varying transformation. For small frequency variations and balanced sinusoidal conditions, these derivatives can be neglected giving an approximate algebraic phasor representation. However, if this condition is not satisfied (i.e., in the presence of broad-band signals), the transformation provides results that have to be carefully interpreted and, in case, compensated.

V. CLASSIFICATION OF CONVERTERS' CONTROLS

A. *Definitions of grid-following and grid-forming converters*

The concept of grid-following and grid-forming converters has been introduced in [87] by establishing an equivalence with the current/voltage nature of the source created by the converter. The idea of grid-supporting had also been introduced and divided in grid-supporting/grid feeding converter (GSGF) and grid-supporting grid-forming (GSGF) [88] when the converter provides ancillary services for the grid. However,

this definition is less useful since it is not based on a fundamental difference between the sources. More recently in [89] a precise definition of the grid-forming converter applied to transmission system has been provided. In what follows, the main distinction between grid-following and grid-forming converter is recalled and specified.

1) Grid-following converters

A grid-following unit is based on a power converter whose injected currents are controlled with a specific phase displacement with respect to the grid voltage at the PCC. As a consequence, the knowledge of the fundamental frequency phasor of the grid voltage at the PCC is needed at any time for the correct calculation of the converter reference currents, whose amplitude and angle with respect to the grid voltage phasor are properly modified by outer control loops so as to inject the required amount of active and reactive power or control the RMS voltage.

2) Grid-forming converters

A grid-forming unit is based on a power converter which controls magnitude and angle of the voltage at the PCC. As a consequence, the knowledge of the fundamental frequency phasor of the grid voltage at the point of connection is not strictly necessary. Depending on the characteristics of the network to which the converter is connected, an isolated system or a slack bus, it is possible by means of additional outer loops to adapt the injected instantaneous active and reactive power also to provide voltage and frequency support. In an isolated system, a grid-forming unit could behave itself like a slack-bus. When connected with other power sources, through an inductive line, the grid-forming converter is controlling the active power by the modification of the angle. The voltage magnitude is independent of the active power control.

B. General considerations of active power control in a voltage source converter

The main aim of a voltage source converter (VSC) is to convert AC power to a DC power and vice-versa. There are several possible topologies. However, in what follows, the possible variants are assimilated in a variable set of three phase voltages v_{m1}, v_{m2}, v_{m3} which are modulated from a DC bus voltage. There are also different types of controls. In any case, a set of three-phase signals in the VSC control homothetic to $v_{ma,ref}, v_{mb,ref}, v_{mc,ref}$, as shown on Fig. 21, can be defined explicitly. The role of the low-level control is to drive the switches of the converter in order to get the average values of v_{ma}, v_{mb}, v_{mc} on a switching time of the transistors in the VSC equal to their respective references $v_{ma,ref}, v_{mb,ref}, v_{mc,ref}$.

The VSC is usually connected to the PCC with a simple inductance. In what follows, the resistance of such inductance is neglected.

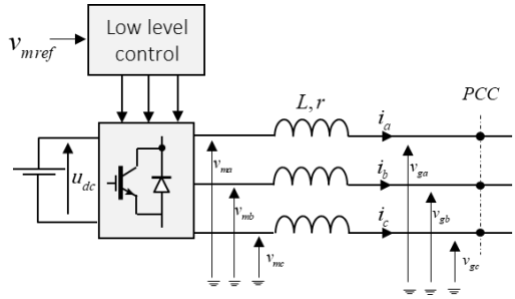

Figure 21. Generic topology of the VSC.

The general organization of the control depends on the choice made for the type of active power control. To develop this idea, a single phase quasi static model of the AC part of the VSC is presented in Fig. 22 with the following phasor variables:

- Grid voltage: $\bar{V}_g = V_g e^{j\delta_g}$
- Modulated voltage: $\bar{V}_m = V_m e^{j\delta_m}$
- Grid current: $\bar{I} = Ie^{j(\delta_g - \beta)} = \bar{I}_P + j\bar{I}_Q$

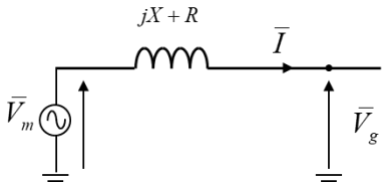

Figure 22. Single phase quasi static model of the VSC connected to the grid.

The angle ψ is defined as: $\psi = \delta_m - \delta_g$ and the active power at the point of common coupling is simply:

$$P = \Re\left(\bar{V}_g \bar{I}^*\right) = V_g I_g cos\beta = V_g I_P \tag{18}$$

In steady state, a formulation based on voltage phasors is possible. In a simplified form, by neglecting resistance R in Fig. 22, this gives the well-known expression:

$$P = \Re\left(\bar{V}_g \left(\frac{\bar{V}_m - \bar{V}_g}{jX}\right)^*\right) = \frac{V_g V_m}{X} sin\left(\delta_m - \delta_g\right) \tag{19}$$

These two expressions are the basis of the two different types of power control in the converters.

C. Grid-following converters control

In the first formulation, the active power is linked with the active current I_P injected at the PCC. The generic active power control scheme is represented in Fig. 23. A power controller defines a reference for the active current I_{Pref}. A current loop is implemented in order to get the active current equal to its reference in steady state. The model of the system is represented by a single gain given by V_g.

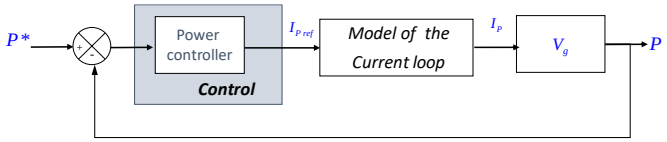

Figure 23. Principle of the active power control with the current.

This model can be considered as valid for the active power controller design as long as the grid voltage is stiff enough.

Fig. 24 recalls the classical structure of the grid-following control. The grid angle is estimated thanks to a phase locked-loop (PLL) and included in the Park's transformation used in control. The active current reference, $i_{d,ref}$, is generated by an outer active power loop. The reactive current reference, $i_{q,ref}$, is the output of a reactive power or voltage control loop(s).

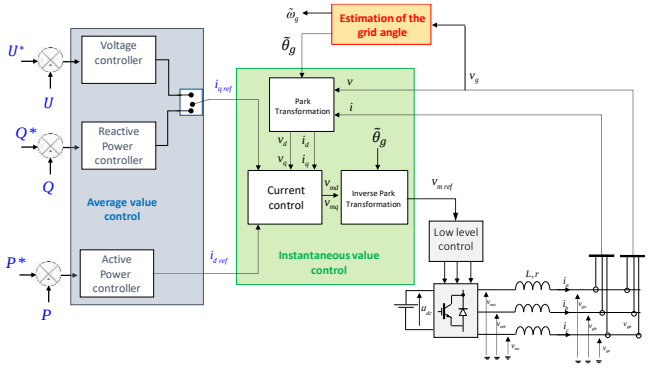

Figure 24. Main scheme of a grid-following control.

D. *Fundamental considerations on grid-forming converters*

The aim of this section is not to propose a review of the various types of grid-forming control (to this purpose the reader may refer to [90]) but to introduce some fundamental thoughts about this control and clearly characterize the influence of the choice of the control on:

- the management of the active power which is, till now, the major aim most of the power electronic converters;
- the type of grid frequency support which is provided by the converter.
- the solicitation on the DC bus source.

The grid-forming control is linked with (19). As observed from (19), the active power is sensitive to the modulated voltage angle δ_m. Hence, as shown on Fig. 25a, the control has to generate an angle reference $\delta_{m,ref}$ for δ_m to control the active power. Since, the grid voltage angle δ_g represents a disturbance for the active power control, a compensation of this disturbance can be included in the control [91]. This control requires that an estimate of the grid angle $\tilde{\delta}_g$ is available.

It is worth noting that the real control is implemented in time domain, so the proposed control has to generate a time-domain angle. Let's define the time domain angles associated with the phasor angles as in (20).

$$\theta_g = \omega_g t + \delta_g \qquad \theta_m = \omega_m t + \delta_m \tag{20}$$

where ω_g is grid frequency, ω_m the modulated voltage frequency. It results in the equivalent time-domain control shown in Fig. 25b with an estimate ($\tilde{\theta}_g$) of the time domain grid voltage angle suitably included. Several solutions can be implemented for this power controller. A possible one is presented in Fig. 26 [91,92] where the controller is an integrator that eliminates the steady state error on the power. The gain m_p modifies the closed loop dynamics. A first order filter is added to mitigate the noise on the measurement and it will also have another role as explain further.

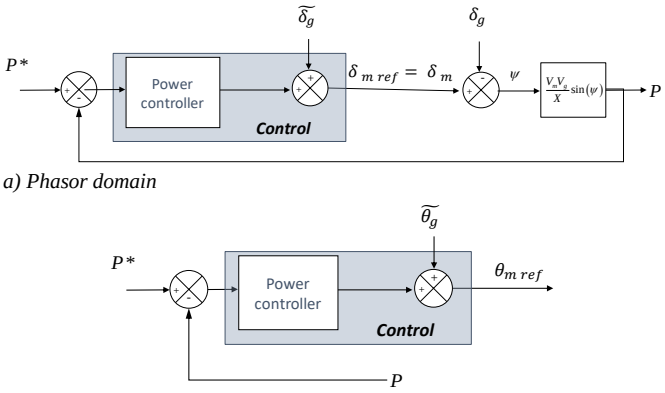

Figure 25. Active power control with the modulated angle voltage.

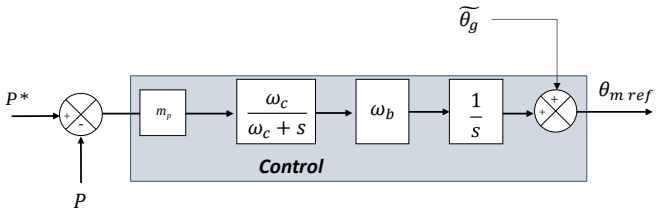

Figure 26. Linear active power controller (scheme A).

In the following, this type of control is named *scheme A*. From this control, it is possible to deduce several variants. All the variants, in general, worsen the accuracy of the active power control but, at the same time, they bring new functionalities. A second possible variant, *scheme B*, is presented in Fig. 27a. The summing junction has been moved to the left and an estimate of the grid frequency is now used. The control is defined in per-unit and, therefore, a conversion has to be integrated in the control to generate the frequency in [rad/s]. ω_b is equal to the nominal grid frequency.

The control shown in Fig. 27a can be rearranged as in Fig. 27b. This structure is known as *virtual synchronous machine* [93,94]. As it can be noticed, the first-order filter introduced above is linked to the inertial effect. Despite a different vocabulary, the fundamental concept for the control is the same. The control parameters can be easily identified and result in the following equation.

$$\omega_c = \frac{K}{2H}, m_p = \frac{1}{K} \tag{21}$$

This second formulation highlights the inertial effect which is brought by this control. However, in steady state, the result is the same as with the previous control, scheme A: $P = P^*$. Since for both controls the active power is regulated in steady state, it is possible to add a classical frequency control.

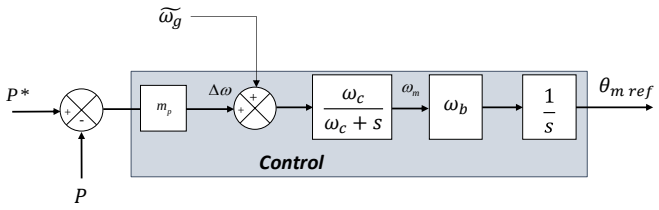

a) First representation: droop control representation

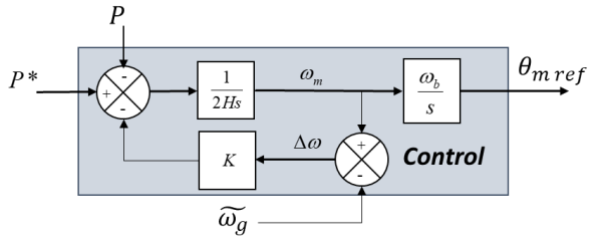

b) Second representation: virtual synchronous machine

Figure 27. Active power control (scheme B).

With this scheme, for a given value of H, a link is established between m_p and ω_c:

$$H = \frac{1}{2\omega_c m_p} \tag{22}$$

This formula will be used further in the examples section. The third variant is very similar to what is found in the literature [87]. The estimate of the grid frequency is replaced by a constant value: ω_{set} (see Fig. 28).

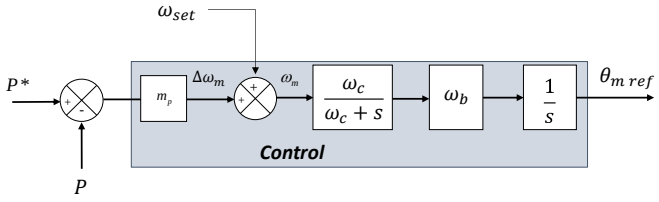

Figure 28. Scheme C for the grid-forming control.

The inertial effect brought by this control is similar to the previous controller, however, the steady state behavior is different. Indeed, since in steady state the modulated voltage frequency ω_m is equal to the grid frequency ω_g, it yields:

$$\Delta\omega_m = \omega_g - \omega_{set} \tag{23}$$

$$P = P^* + \frac{1}{m_p}\left(\omega_{set} - \omega_g\right) \tag{24}$$

This static equation highlights a correlation between P and the grid frequency: as soon as the grid frequency changes, the active power is adjusted [95]. This is a primary frequency support, which is inherent to this type of control. Hence, m_p has to be adjusted with respect to the frequency support requirement but, at the same time, it has also an influence on the response of the power control loop. Depending on the chosen inertial value, it may be needed to add a derivative action in the loop to stabilize the closed-loop system.

Fig. 29 presents the general structure of the grid-forming control for schemes B and C presented as a virtual synchronous machine configuration. It is worth noting that the voltage magnitude control has been also added. In some situations, a very simple reference on the d axis is sufficient to control the voltage at the PCC. In power transmission systems, the Thévenin equivalent grid input resistance is low compared to the reactance, so a damping transient resistance has to be added to damp the natural 50 Hz poles of grid [95,96]. In case of overcurrent, a virtual impedance can also be adjusted to limit the current. Note that these schemes can be applied either on a Modular Multilevel Converter (MMC) or VSC connected to the grid with an LC filter provided that the internal current and voltage loop are correctly tuned [97-99].

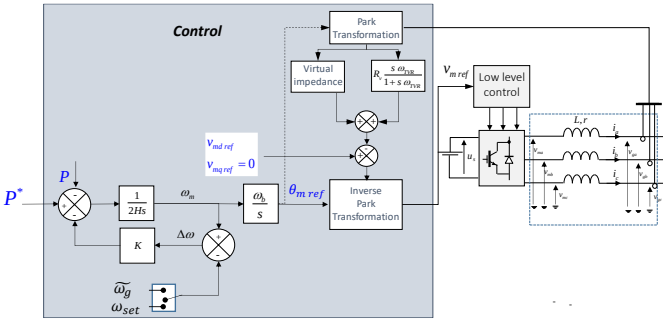

Figure 29. General structure of the grid-forming control.

This section has introduced three main grid-forming controls. Simulation results presented in the next sections illustrate the properties of these different controls.

E. Examples

In the simulation model, the grid forming converter is supposed to be connected to an external system represented by a Thévenin equivalent as shown on Fig. 30. The SCR can be modified by adjusting the grid inductance (L_g), the resistance (r_g) is considered to be negligible. The magnitude of the voltage source is constant. In a first step, the grid frequency is considered constant.

.

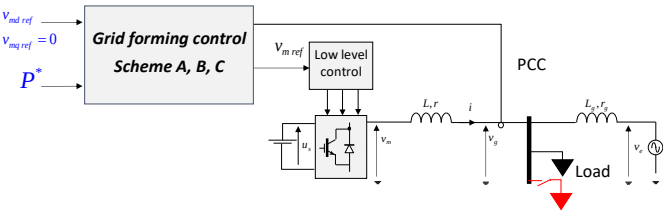

Figure 30. Connection of the grid-forming converter to a Thévenin equivalent.

The aim of scheme A is only to control the active power. The value of the gain m_p can be modified to adjust the dynamics of the system as shown on Fig. 31 where a step is applied on the active power reference.

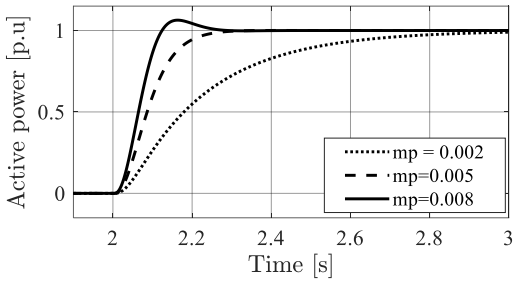

Figure 31. Dynamic response of a grid-forming control (scheme A) for various values of m_p.

The value of ω_c has been chosen to be 30 rad/s. This control reveals excellent robustness against grid impedance variations as demonstrated in [91,92]. As highlighted in Fig. 32, this control mitigates the sensitivity of the grid-following converter with respect to the variation of SCR [60,100].

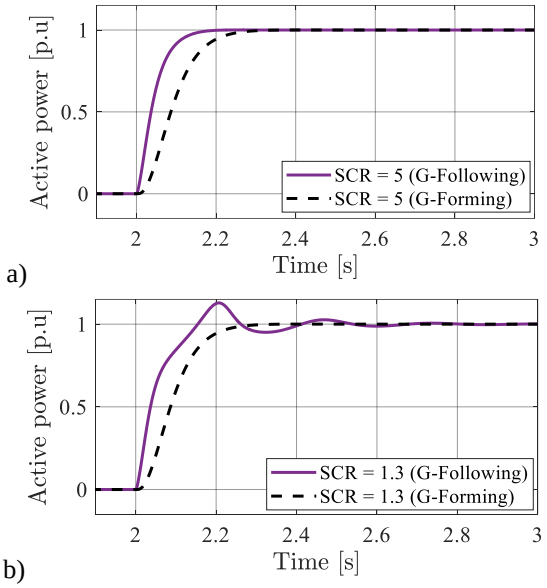

Figure 32. Comparison of grid-following and grid-forming control (Scheme A) for two SCR values: a) SCR = 5, b) SCR = 1.3.

In scheme B, an inertial effect is provided. The gain m_p cannot be chosen with respect to the dynamics anymore since the product $\omega_c m_p$ is relative to the inertial effect as already reported. Hence, to maintain a given inertial effect, the value of ω_c has to be adjusted when modifying m_p. Fig. 33 shows the results for a value of 5s. It shows that the increase of m_p may induce large overshoots. It is possible to find a value for m_p that results in an appropriate overshoot. However, the response time for the active power may be slightly slower than scheme A.

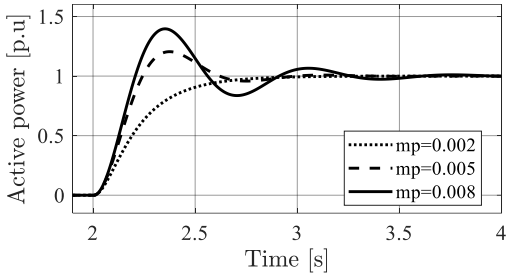

Figure 33. Effect of the choice of m_p on the dynamics of a grid-forming control (Scheme B) H = 5s.

In scheme C, the gain m_p is relative to the frequency support. As previously explained, its value has to be coordinated with the other sources connected to the same grid in order to provide a good load sharing in case of frequency support. Increasing the inertial effect is possible only by decreasing ω_c. This has a large effect on the stability as highlighted on Fig. 34. It is the reason why this type of control has often been referred as *zero inertia* (VSMOH) [101]. However, a derivative effect can be added on the active power in order to stabilize the system [61].

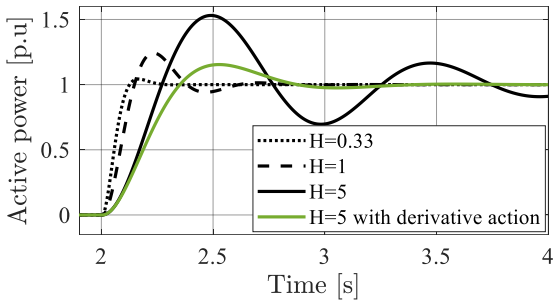

Figure 34. Effect of the increase of H on the stability of the system (scheme C).

In many applications, an LC filter is added between the converter and the connection impedance as shown Fig. 35. The grid forming control is unchanged, however, a specific design of the current and a voltage loop have to be implemented to control the internal dynamics of the filter [97]. Hence, the grid forming control is calculating a reference angle for the voltage, e_g, across the capacitor ($\theta_{g\,ref}$).

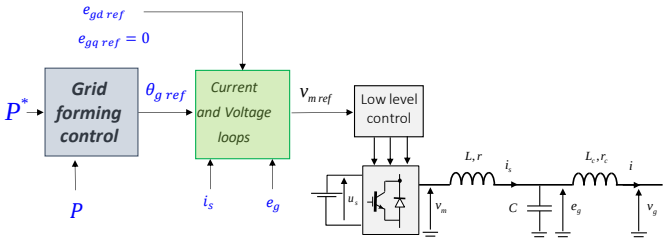

Figure 35. Connection of the grid forming converter with an LC filter.

In Fig. 36, simulation results compare the dynamics of the system with an R, L connection and an LCL one with current

and voltage loop. It can be seen that the difference is negligible.

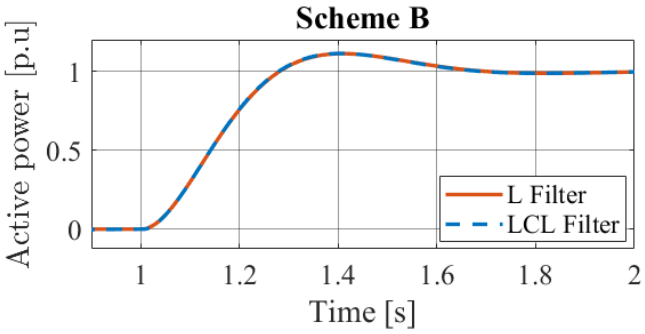

Figure 36. Comparison of the grid forming converter with R, L or LCL connections (scheme B).

The transient stability of the grid-forming control has been tested for various events which would induce an overcurrent in the converter. The current limitation is obtained first with a saturation on the current reference and then the introduction of a virtual impedance which increases the critical clearing time [102]. After the fault, the re-synchronization is operated with no external signals. As soon as the current decreases below a given limit, the virtual impedance is removed. In Fig. 37, the different controls are compared after the bolted fault at the PCC.

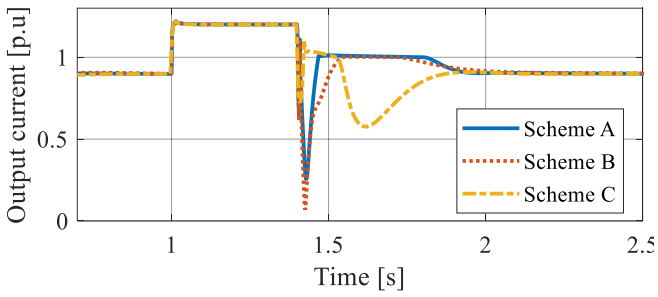

Figure 37. Short circuit at the PCC.

During the fault, it may be interesting to decrease the value of m_p in order to enhance the critical clearing time. To highlight the inertial effect, a small variable frequency system has been implemented. The voltage source frequency (ω_e) is defined by the system presented in Fig. 38. It represents an equivalent electrical system with an inertia H_{eq} and a dynamic represented by a lead lag filter T_N, T_D. A frequency support is implemented with a droop control.

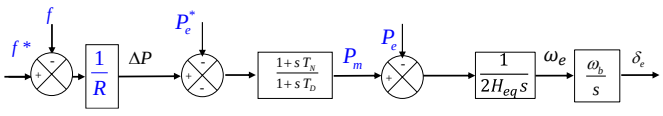

Figure 38. Equivalent system for the definition of the voltage source frequency.

In a first step, scheme A, and B are compared in terms of inertial effect. The outer loop for frequency support is not activated for the grid-forming control. To modify the grid frequency, a load variation is applied at the node located at the PCC (see Fig. 30). As it can be noticed on Fig. 39, scheme A does not provide any inertial effect whereas the power increases with scheme B to counteract the frequency variation.

In a second step, schemes B and C are compared in terms of inertial effect. Since a droop effect is inherently embedded in the scheme C, the outer frequency loop is activated in the scheme B to have the same behavior. In Fig. 40, the simulation results are presented for both controls with the same value of inertia and the same droop. These results show that the dynamic behavior of these controls is very similar.

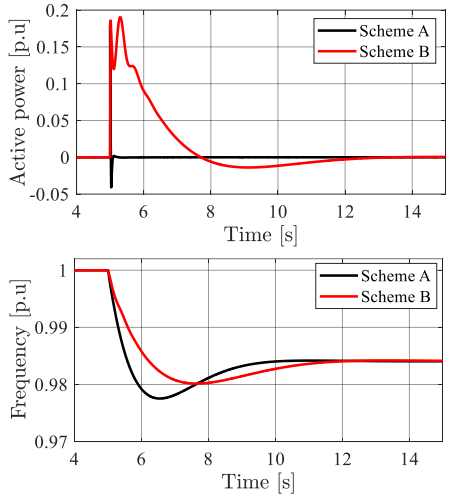

Figure 39. Comparison between schemes A and B in case of grid frequency variation.

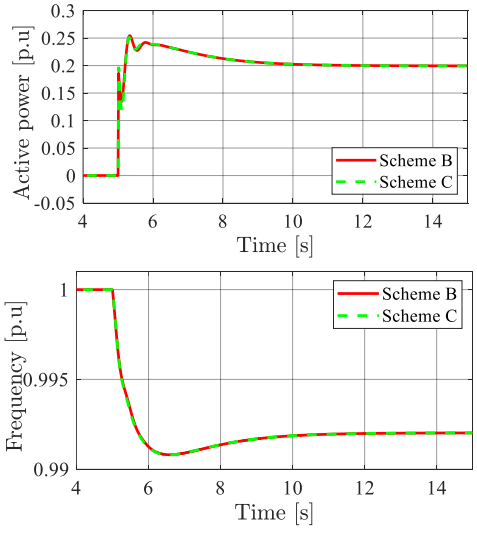

Figure 40. Comparison between schemes B and C in case of grid frequency variation.

F. *Synthesis on grid forming control*

Various conclusions can be drawn from the study of the three types of grid forming control which have been introduced. The first one is about the frequency support. In scheme A, the modulated voltage angle is following the grid voltage angle thanks to the PLL. Hence, the active power is independent from the grid frequency variation which means that no frequency support is inherently brought by this type of control. In scheme B, the PLL is only providing an estimate of the grid frequency and the inertial effect is added afterwards. In scheme C, the dynamic information about grid frequency is replaced by a constant value adding a frequency droop. It can be concluded that a very small difference in the control may have a very large influence on the general behavior of the power converter and, then, on the DC bus solicitation. Indeed, in the two last controls, since an inertial effect has to be provided, there is the need to understand the origin of the extra power provided by the converter in case frequency drop: either it comes from the DC source, or a suitable storage element placed on the DC bus. This question is even more important in case of a permanent frequency support induced by a droop control on the frequency.

The second conclusion is about the question of active power dynamics when the grid frequency is fixed since it may be an important requirement especially for HVDC application. It has been shown that, depending on the choice on the control, the response time can be chosen (scheme A) or a consequence of other choices. In scheme C, for example, the inertia is first chosen. Then, the gain m_p is adjusted with respect to the load sharing capabilities and the derivative action is used to damp the dominant poles. The response time is then a consequence of these choices. In case of a back-to-back or HVDC application, the question of the DC bus voltage control is also relevant. Indeed, a poor response time on the active power would induce an even worse control on the bus voltage.

A third point is about the use of PLL in the grid-forming control. Indeed, the PLL is often associated with the idea of a poor robustness in case of weak grids. This effect, which is noticed in case of a grid following converter, is not taking place for the grid-forming control since the role of the PLL is not the same.

All the simulation models are available for the reader in open source (see [103]). It should be highlighted also that all the results obtained in simulation have been verified via the experimental setup described in [104]. In the existing literature other types of control have been proposed. The synchronverter is very similar to the VSM scheme. The main difference is about the modulated voltage magnitude which is imposed as proportional to the modulated frequency, to mimic the emf of a real synchronous machine. Matching control [105] and virtual oscillator [106] propose very different algorithms to manage the modulated voltage. However, in the case of transmission system applications, the dynamics which are obtained are very similar to the droop control as reported in Migrate EU project [104].

To conclude on the various types of grid forming control, here is a list of question which should be asked for all the possible solutions of control. What is the active power dynamics in case of a fixed frequency grid ? Is there an inertial effect ? Is the proportional frequency support compulsory or optional ? What is the robustness of the control with respect to the SCR ? How this grid forming converter is protected against over current ? Is this control implemented for R, L connection and/or LC filter connection ? Some further questions can also be added such as the number of parameters to characterize the controls and also the ability to integrate some grid forming converters in large power system study. Even if it is always possible to improve existing controls, it can be noticed that classical VSM is already gathering many of the good properties possessed by this control.

G. *Effects of synchronization on small-signal stability*

As highlighted in Fig. 24, a dedicated unit identifying the grid voltage angle and calculating a proper phase shift of the converter currents for the injection of the defined amount of active and reactive power, is requested for the proper operation of a grid-following converter. Grid synchronization has been a crucial issue since the early stage of development of power electronics-based converters, and several techniques have been proposed. These can be classified into two main categories: frequency-domain and time-domain approaches. Frequency-domain approaches are based on some discrete implementations of the Fourier analysis, such as the DFT and recursive DFT, while time-domain approaches are based on adaptive feedback loops, enabling an internal oscillator to track the component of interest of an external signal. The commonly adopted solution is the use of a PLL and the synchronous reference frame PLL (SRF-PLL) is among the most widely proposed techniques.

Recent studies have shown the negative effects of synchronization units, often implemented by means of PLLs, on the small-signal stability of grid connected converters [53]. Fig. 41 shows the results of the Monte-Carlo based analysis performed in [53], and analyses the effects of the interactions among synchronization units of GFL converters operating nearby. It has been demonstrated that not only the stability margin of a GFL converter is reduced when other converters of the same type operate in its proximity, but also that the magnitude of the interactions among synchronization units of GFL converters are strongly accentuated by the decrease of the grid short circuit ratio (SCR).

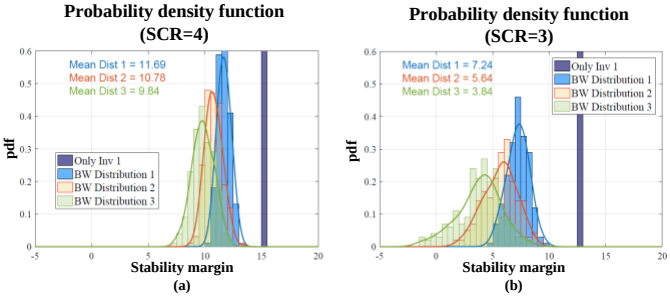

Figure 41. Results of the Monte-Carlo analysis performed in [53] in order to study the effects of the interactions among synchronization units of grid-following converters operating nearby: (a) SCR=4, (b) SCR=3.

On the contrary, according to the general control structure presented in Fig. 42, a grid-forming converter is able to self-synchronize to the grid without the need of a dedicated unit. As a consequence, the issues related to the PLL common to GFL converters are completely avoided in GFM converters. Furthermore, the study illustrated in [60], demonstrates that, due to their intrinsic behavior as voltage source behind impedance along with their ability of self-synchronization, GFM converters are actually suitable for weak grid applications. The results of the robust stability analysis performed in [60] by means of structured singular values are reported in Fig. 42. The μ-analysis is a useful tool for investigating control robustness, and it is particularly suitable for multiple-input multiple-output (MIMO) system analysis. The approach consists of including plant uncertainties in the stability analysis of a control by defining a frequency-dependent uncertainty function, so that stability is assessed for a set of possible plants, rather than for a specific configuration. Possible causes for system uncertainties can be represented by neglected dynamics of sensors and actuators, parameter uncertainties, or unknown behavior of other components in the system. This turns to be particularly suitable for studying stability of grid-connected converters in power electronics-dominated systems. In fact, the equivalent grid impedance seen at the converter terminals is often modelled as a resistive inductive element, whose parameters are estimated according to indications about the X/R ratio and the short-circuit power at the connection point. However, although excursions of these parameters within defined ranges are often considered, the usually unknown frequency behavior of the other converters operating nearby might substantially affect the equivalent grid impedance seen by the converter. The approach allows calculating a factor (the so-called μ-factor), whose inverse can be interpreted as a stability margin for the investigated system. A μ-factor below the unity indicates that the control is robust against all the plants identified by the chosen uncertainty function. Fig. 42 shows the effects of the SCR on the calculated μ-factor for the case of a VSM connected to the grid by means of an LCL filter. The different curves shown in Fig. 42 show that the increase of the grid impedance causes a decrease of the highest peak of the μ-factor, indicating therefore an increase of the robust stability of the converter.

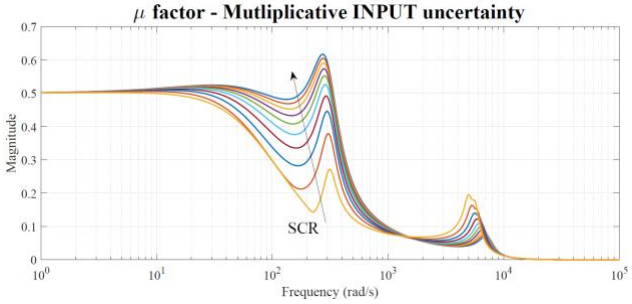

Figure 42. Results of the μ-analysis performed in [60], showing the effects of the SCR variation on the robust stability of a grid-forming converter.

VI. APPLICATIONS

The previous sections of the paper focused on the description of the main modelling challenges power systems in the presence of large amounts of CIG. The goal of this section is to transpose these analyses into application examples associated to power systems of significant size and complexity.

A. *Phasor analysis of power systems experiencing large contingencies*

In this section we would like to assess the appropriateness of a phasor-based representation to compute the electrical instantaneous power of a benchmark power grid during a contingency. We apply the same process illustrated in section IV.A to the dynamic model of the IEEE 39-bus power system, also known as 10-machine New-England power system represented in Fig. 43. The simulated power system is characterized by a nominal voltage of 345 kV, and consists of 39 buses, 10 generators and 19 loads. The overall system installed capacity is 10 GW. In order to consider the effects of CIG, we modify the benchmark by replacing 4 conventional synchronous generators with wind farms, for a total wind installed capacity of 4 GW. Wind and load profiles are derived from real measurements. The open source network model used here is reproduced in Simulink and the simulations are run using the Opal-RT eMEGAsim real-time simulator. The model is available open-source [107] along with a thorough description of the data used in the model.

In this case, we simulate the outage of generator G6, with a total tripped power of 800 MW that triggers a strong system dynamic response resulting in an average frequency nadir close to 47.5 Hz, peak values of RoCoF of +8 Hz/s and -7 Hz/s and an average RoCoF (from the pre-contingency state to the frequency nadir) of -0.5 Hz/s. The generator is tripped at t=180 s and the transient lasts for roughly 100 seconds. Fig. 44 shows the results of the phasor-based analysis performed at bus 21 (similar results hold for all the buses in the network) where we reconstructed the phase-to-ground voltages and the load currents using the same approach of section IV.A. Voltage and current simulated signals are used to estimate the three-phase instantaneous power absorbed by the load at node 21. As it is shown in Fig. 44, the phasor-reconstructed waveform of the voltage is inaccurate with respect to the simulated one due to a superposed frequency ramp and an amplitude modulation. As a consequence, during the whole transient, the phasor representation does not provide a truthful estimation of the instantaneous electrical power leading to errors in the order of 400 MW (i.e., 40% with respect to the true 3-phase power absorbed by this load). This result is of course associated to the extreme system dynamic we are studying suggesting that, as the dynamical response is system dependent, a phasor-based analysis should be quantitatively benchmarked against the corresponding time-domain analysis in order to verify its appropriateness.

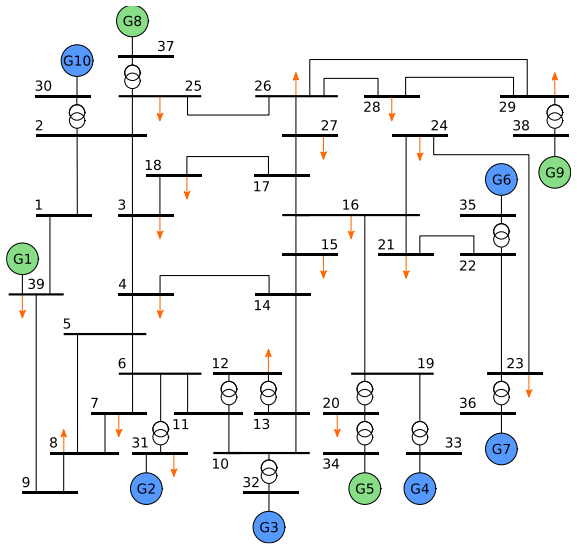

Figure 43. Diagram of the modified IEEE 39-bus power grid simulation model [107] characterized by nominal voltage of 345 kV and total installed capacity of 10 GW. The model consists of 6 synchronous generators (blue circles), 4 wind farms (green circles) and 19 loads (orange arrows).

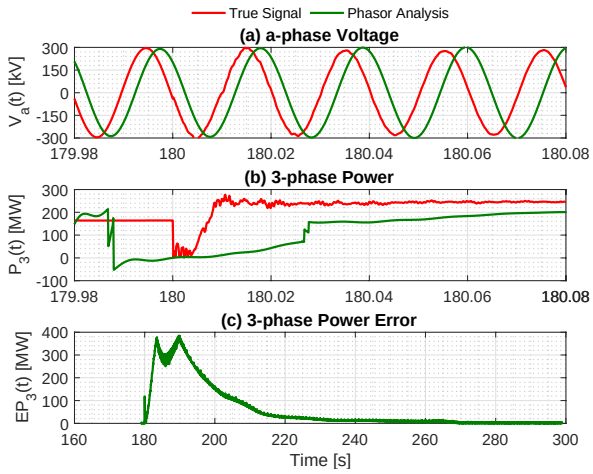

Figure 44. Analysis of the phasor-reconstructed signals during a contingency happening on the IEEE 39-bus system (outage of generator G6): a) true (simulated) and phasor-reconstructed phase-to-ground voltage waveforms, b) error of the phasor-reconstructed three phase power.

B. Protection and control for systems with high levels of CIG

The characteristics of systems with high penetration of grid interfaced inverters, GFL or GFM, are substantially different from conventional systems with primarily synchronous generators both in terms of fault current levels and fault current components, i.e., DC offset, negative and zero sequence components and duration. Specifically: (a) generators/step-up transformers generate fault current several times greater than rated currents and significant levels of DC offset, negative and zero sequence currents; legacy protection functions depend on these characteristics to reliably detect faults, coordinate the various legacy protection functions and protect the system; (b) fault current contributions from inverters are comparable to load currents and do not include, or produce much lower negative and zero sequence currents; many legacy relays require high fault current to detect a fault and use the negative or zero sequence component as a polarizing quantity to detect fault direction; these relays may malfunction under these conditions; and (c) many grid interfaced inverters connect variable amount of renewable energy resources to the grid resulting in frequent configuration changes altering the network topology; this reality makes the process of coordinating legacy relays very challenging and many times unsolvable resulting in mis-coordinated schemes.

To address the above issues, the dynamic state estimation-based protection (EBP) method (a.k.a. setting-less protection, see Fig. 45) has been introduced in [108]. It does not need complicated settings and no coordination is required with other protection functions. The EBP examines the consistency between the measurements and the dynamic model of the protection zone. The EBP has been inspired from differential protection which simply monitors Kirchoff's current law of a protection zone. EBP extents this concept to monitor all physical laws obeyed by the protection zone, and therefore will not be affected by external variations such as frequent changes of sources, level of fault currents, content of fault currents and/or loads. Therefore, it is immune to the characteristics of inverter interfaced generation.

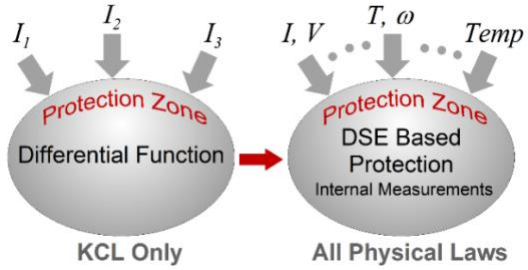

Figure 45. Conceptual Illustration of the Dynamic State Estimation Based Protection (EBP).

In dynamic EBP protection, all existing measurements in the protection zone are utilized: currents and voltages at the terminals of the protection zone, as well as voltages and currents inside the protection zone (as in capacitor protection) or speed and torque in case of rotating machinery or other internal measurements including thermal measurements. These measurements should obey the physical laws for the protection zone (for example, physical laws such as KCL, KVL, motion laws, thermodynamic laws). This principle means that the measurements should satisfy the dynamic model of the protection zone as long as the protection zone is free of faults. When there is a fault within the protection zone, the measurements would not satisfy the dynamic model of the protection zone. This distinction is a powerful, secure and reliable method to identify internal faults and block any external faults. A systematic approach to verify whether the measurements satisfy the mathematical model is the dynamic state estimation. The resulting method is a dynamic state estimation-based protection (EBP). When an internal fault occurs, even high impedance faults or faults along a coil, for

example, the dynamic state estimation reliably detects the abnormality and a trip signal is issued. The method is immune to the presence or penetration level of CIGs. This basic approach has been presented for specific cases [109]-[114].

The EBP method requires a high-fidelity mathematical model of the protection zone, the measurements and the dynamic state estimation algorithm.

The dynamical model of the protection zone is a set of differential and algebraic equations. In general, it will be a multi-physics model, for example, for transformer protection, the model will be the electro-thermal model of the transformer. The proposed method starts with this model and utilizes a *quadratization* procedure which reduces any higher order nonlinearities to no more than second order by the introduction of additional variables, if necessary (if model is linear or quadratic this process is not needed). This transformation does not change the model. We refer to this model as the quadratized dynamic model of the protection zone (QDM). The form of the QDM is given below in matrix format.

$$
\begin{aligned}
i(t) &= Y_{eqx1}\mathbf{x}(t) + D_{eqxd1}\frac{d\mathbf{x}(t)}{dt} + C_{eqc1} \\
0 &= Y_{eqx2}\mathbf{x}(t) + D_{eqxd2}\frac{d\mathbf{x}(t)}{dt} + C_{eqc2} \\
0 &= Y_{eqx3}\mathbf{x}(t) + \begin{Bmatrix} \vdots \\ \mathbf{x}(t)^T\langle F^i_{eqxx3}\rangle\mathbf{x}(t) \\ \vdots \end{Bmatrix} + C_{eqc3}
\end{aligned}
\tag{25}
$$

The first matrix equation expresses the through variables, $i(t)$, of the protection zone; note that in a case of an electrical system the through variables are simply the currents at the terminals of the protection zone, for rotating machines it may also include torque, and for electro-thermal models it may include heat flow. The variables contained in the array $\mathbf{x}(t)$ represent the state of the protection zone; for a purely electrical system, the state variables are the voltages at the various nodes of the system and the matrix Y_{eqx1} the resistive admittance matrix. The dynamics of inductors, capacitors, rotating mass and other such components are represented with the differential terms. Note also the states for rotating machines may include speed and for electro-thermal models will include temperatures. The second matrix equation represents the internal equations of the system; in case of an electrical system, these equations would be KCL and KVL for internal electrical nodes and/or electrical loops of the system. Finally, the third matrix equation represents the nonlinear relationships among the states of the protection zone. Detailed information can be found in [111] through [114].

The measurements are expressed as functions of the protection zone state, $\mathbf{x}(t)$. These functions may include linear, quadratic and/or differential terms:

$$
\mathbf{z}(\mathbf{x}) = Y_{mx}\mathbf{x}(t)\begin{Bmatrix} \vdots \\ \mathbf{x}(t)^T\langle F^i_{mx}\rangle\mathbf{x}(t) \\ \vdots \end{Bmatrix} + D_{mx}\frac{d\mathbf{x}(t)}{dt} + C_m \tag{26}
$$

where $\boldsymbol{z}(t)$ are the measured quantities. These measurements may represent any measurable quantity of the system, for example voltage, current, speed, temperature.

Any protection zone model can be casted into the above syntax. Models of transformers, lines, capacitor banks, motors, generators units have been developed using the QDM syntax. This syntax enables a full object orientation in all subsequent computations.

Using the protection zone and measurement model in QDM syntax, the dynamic state estimation is performed by an algorithm that is identical for any protection zone (i.e., it is object-oriented). Three alternate approaches have been implemented and tested for the dynamic state estimation algorithm: (a) extended Kalman filter, (b) constrained optimization method where the constraints are the second and third matrix equations in (25), and (c) unconstrained optimization method where the above mentioned constraints are relaxed and enforced via penalty functions [110].

To illustrate the method and exemplify the merits of the approach, an example protection system is presented here. The example compares the performance of a high-end protective relay to the performance of the EBP for a circuit in a microgrid that includes many inverters and it is designed as a five-wire system (there phases, neutral and ground). The microgrid is shown in Fig. 46. The circuit under protection is the circuit between buses I and II. The circuit cross section is also given in the figure, showing the three phases, the neutral and the ground in the form of the conduit.

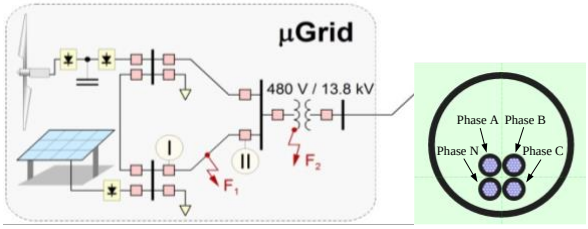

Figure 46. Example microgrid and circuit under protection.

Assuming that two distance relays protect the indicated circuit at the two ends of the circuit, we simulate a single-phase to ground fault in the middle of the circuit and observe the response of the relays. The response is illustrated in Fig. 47. Note that, even if the fault is in the middle of the circuit, the distance relay "sees" the impedance way outside the relay characteristics (red star in Fig, 47). This wrong performance is the result of the inverter characteristics and the grounding design of the five-wire system. Note that if the model is simplified and symmetrical components are used, then the relay will see the impedance at zone 2 characteristic (blue star in Fig, 47). This performance is still wrong since the fault is in the middle of the circuit and the relay should have seen the fault inside the zone 1 characteristic.

Now we simulate the operation of the EBP for the same circuit and the same fault. The results are shown in Fig. 48. The figure illustrates the electric current waveforms (top two

traces), the residuals computed by the dynamic state estimation (mid traces) and the confidence level (bottom trace, probability that the measurements fit the dynamic model). Note once the fault occurs the confidence level drops to zero indicating an internal fault. Once the fault is detected the EBP relay uses user directives to trip the circuit (user defined delays and transfer trip if required). Note also in this case, the fault current before and after the fault are not very different as the inverters limit the fault current.

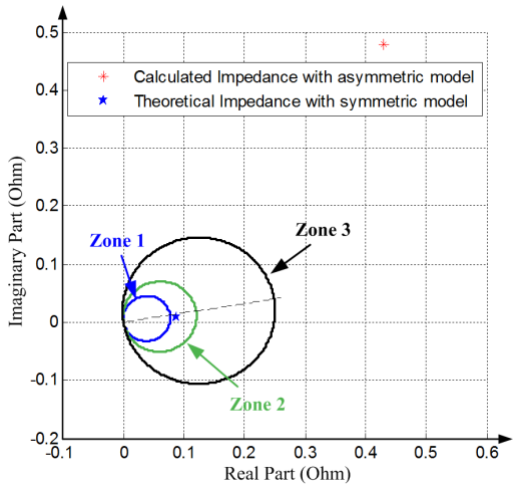

Figure 47. Performance of distance relay for a fault in the middle of the circuit I-II (see Fig. 46).

This example illustrates that in the presence of inverters, legacy protection may mis-operate (in this case will not trip a fault in the middle of the circuit under protection) while the estimation-based protection will reliably detect the fault and trip the circuit, even if the fault current levels are quite low.

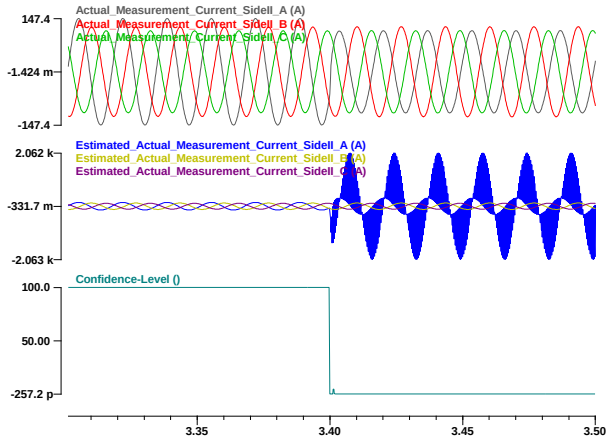

Figure 48. EBP Results: fault in the middle of circuit I-II (see Fig. 46).

C. *Case study on transient stability*

A three-machine nine-bus equivalent system [115] shown in Fig. 49 was used to validate the performance of the converter model developed in [116] along with its associated controls in a commercial transient stability analysis package. This system consists of 9 buses, 3 generators and 3 static loads. Though the size of the system is small, it is sufficient to showcase a variety of stability concepts. The power flow solution of this network, power consumed by the load at buses 5, 6 and 8 and the dynamic data is given in [115].

The results shown were a part of the work done in [117] and the reader can find more details in this reference. Two different positive-sequence converter models were used in the simulation. The first model is the one available in GE PSLF [118]. This model is referred to as the boundary current representation of the converter. The second positive-sequence converter model is a controlled voltage source converter model developed in [116].

With the loads treated as constant admittances, the load at bus 6 was increased by 10MW at t = 5s. A comparison of the performance of the two positive-sequence converter models with a point on wave representation of a converter with all controls and phase-locked-loop representation using PLECS was conducted.

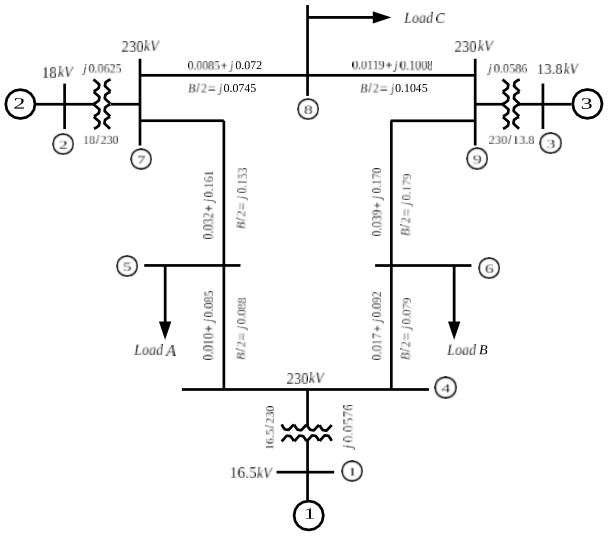

Figure 49. Three machine nine bus equivalent.

In the first scenario, only the machine at bus 1 was replaced with a converter while the machines at buses 2 and 3 were retained as synchronous machines with associated governors and static exciter models. Fig. 50 shows the active power output of the converter at bus 1. The PLECS response has been compared with both the voltage and boundary current representation of the converter in positive-sequence. The inset figure shows the response of the models at the instant of disturbance. It can be seen that both the proposed controlled voltage source representation of the converter model and the PLECS response capture the near instantaneous response achievable by the converter while the boundary current representation is unable to do so. The difference in the peak value between the voltage source representation response and the PLECS response can be attributed to the fact that the time step of simulation is much smaller in PLECS which allows for the change in the internally generated converter voltage upon

recognition of the disturbance. In the positive-sequence simulation however, at the instant of disturbance, the internally generated converter voltage is constant while the terminal voltage changes.

Further, the dissimilarity can be attributed to the difference between the point on wave modelling in PLECS wherein a differential $R + sL$ model is used in PLECS for the filter inductor whereas in the positive sequence phasor model the filter is represented by its algebraic fundamental frequency resistance and reactance in the Thévenin impedance.

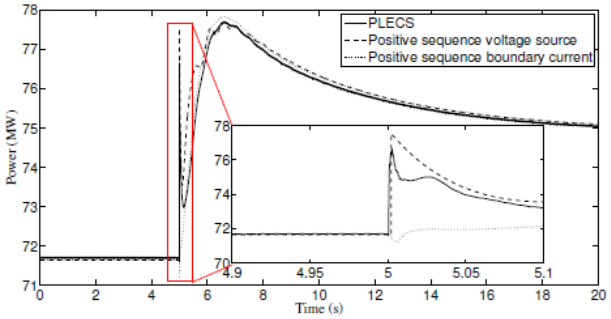

Figure 50. Comparison of the active power output at bus 1 between PLECS and the user defined model in PSLF with synchronous machines at buses 2 and 3.

The instantaneous 3 phase voltage and current waveforms at the converter terminals are as shown in Figs. 51 and 52 respectively. These figures show that there is a negligible change in the terminal voltage while the converter current rises near instantaneously to meet the demand.

The magnitude of the converter current output from PLECS is compared with the positive sequence simulations as shown in Fig. 53. It can be seen that the near instantaneous response achievable by the converter is captured by voltage source representation of the converter.

The reactive power response is shown in Fig. 54. It can be immediately observed from this figure that the voltage source representation response is the more acceptable positive-sequence phasor approximation to the point on wave simulation. From the inset of the figure it can be seen that the reactive power trajectory of the boundary current simulation is evidently inconsistent with the result from the PLECS simulation. The trajectory produced by the voltage source positive-sequence model, while not reproducing the slight oscillatory component of the electromagnetic response, is consistent with the PLECS simulation in the direction of its initial change. This difference in the response at the instant of disturbance justifies the use of the voltage source representation as the model of choice for the simulation of large systems. Due to the absence of any connection to ground at the terminal bus of the converter in the positive-sequence boundary current representation, the network solution results in an instantaneous large voltage dip at the instant of disturbance. This results in the initial change of reactive power in the direction opposite to the PLECS simulation.

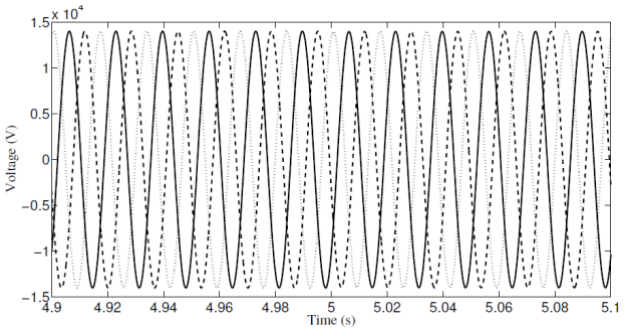

Figure 51. Phase voltage waveforms at the converter terminal from PLECS

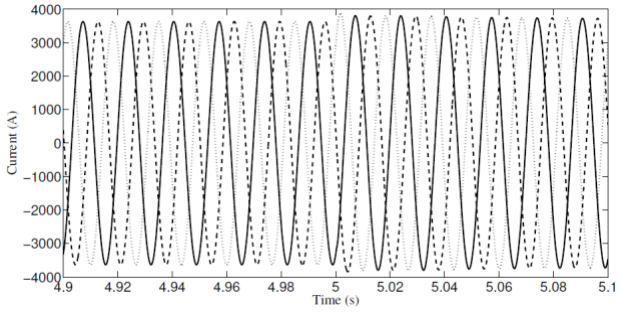

Figure 52. Line current waveforms at the converter terminal from PLECS

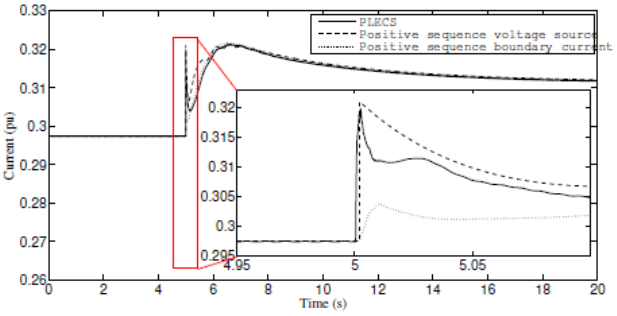

Figure 53. Comparison of the current output at bus 1 between PLECS and the user defined model in PSLF with synchronous machines at buses 2 and 3.

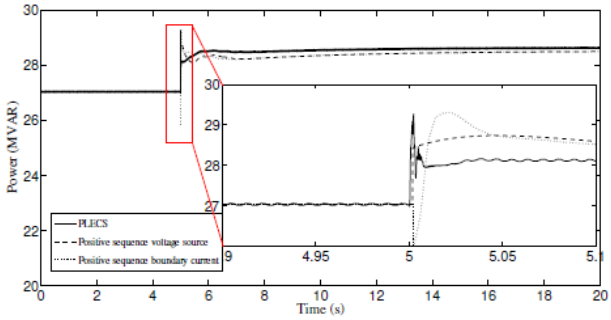

Figure 54. Comparison of the reactive power output at bus 1 between PLECS and the user defined model in PSLF with synchronous machines at buses 2 and 3.

It is to be noted that no PLL is represented in the positive sequence simulations and the time step used is ¼ cycle of 60 Hz. The simulations pose no problem since the implicit assumption is that the PLL would have acted within this time scale.

In order to examine an all CIG system, the machines at buses 2 and 3 were also replaced with both forms of the positive-sequence converter model. The same load increase of 10 MW at bus 6 is simulated. The active power outputs from the converters is shown in Fig. 55. With the final steady state values being almost the same, the behaviour of the models at the instant of disturbance becomes the deciding factor. It can be seen that in an all CIG system too, the boundary current representation response instantaneously moves in a direction opposite to what would be expected while the response from the voltage source representation is as expected and it conforms to the power sharing characterized by the equation given below.

$$P_{i\Delta}(0^+) = \left(\frac{P_{sik}}{\sum_{j=1}^{n} P_{sjk}}\right) P_{L\Delta}(0^+), i = 1,2,\dots,n \quad (27)$$

$$P_{sik} = V_i V_k (B_{ik} cos\delta_{ik0} - G_{ik} sin\delta_{ik0}) \quad (28)$$

where

- $P_{i\Delta}(0^+)$ is the share of load change picked up by source at bus *i*;
- P_{sik} is the synchronizing coefficient between buses *i* and *k*;
- $P_{L\Delta}$ is the load change;
- V_i is the terminal voltage magnitude at bus *i*;
- $B_{ik} - G_{ik}$ is the grid admittance between buses *i* and *k*;
- δ_{ik0} is the initial terminal voltage angle difference.

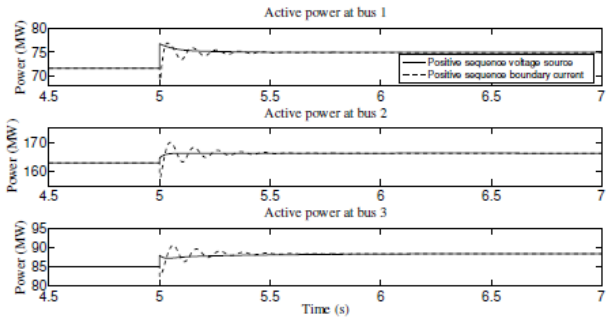

Figure 55. Active power output of the converters for an all CIG system with increase in active power load.

The above distribution of the power impact is based on electrical distance between the internal voltage source of the converter and the disturbance location and the equations above provide the instantaneous response of a converter at bus *i* for an impact at bus *k*. This test demonstrates that the voltage source converter model with the appropriate droop characteristics in the active and reactive control loops facilitates the response of the CIG to respond like a synchronous generator in response to power impacts. Large scale simulations of an all CIG case for the wind energy conversion systems has been conducted in [119] for a number of different disturbances using the controlled voltage source positive-sequence model and are not repeated here.

D. Case study: zero and low-inertia approaches of an offshore wind power hub

1) Context

The wind at sea is a major resource of renewable energy yet to be exploited. More steady wind and no intrusion into densely populated areas are among the advantages of offshore wind farms over their onshore counterparts. While more and more wind farms are put in operation at moderate distances to shore (allowing their connection through AC cables), there remains a huge potential for wind energy extraction from more distant locations in the seas/oceans.

This opportunity prompted the setting up of a Danish, Dutch and German consortium to explore the possibility of developing a wind power hub in the North Sea [120]. Preliminary studies deal with the feasibility of building (initially one, subsequently several) artificial islands to gather the power from thousands of offshore wind turbines with a total capacity approaching 36 GW [121]. The length of the submarine cables makes HVDC transmission the only choice.

The second purpose of such an offshore wind power hub (OWPH) is to allow for power exchanges between the onshore AC grids to which the islands would be connected (hence the term "hub"). These connections would make up an overlay DC grid connecting the (possibly asynchronous) AC networks

The modelling, dynamics, control and stability of an OWPH is a topic of the *multiDC* research project, devoted to "Advanced control and optimization methods for AC and HVDC grids" (please refer to www.multi-dc.eu). Sample results from that project are presented here.

2) Topology and converter types

A generic OWPH structure is outlined in Figs. 56 and 57. Several artificial islands are considered in order to accommodate the large number of wind turbines, while keeping a reasonable distance between the wind turbines and the collecting islands.

A first option is the multi-terminal HVDC grid sketched in Fig. 56 [122, 123]. One well-known issue is to deal with faults affecting the DC grid. Shutting down all the AC/DC converters, i.e. de-energizing the whole HVDC grid, cannot be envisaged. An alternative would be to operate it in disconnected sub-grids [123] and shut down only the faulted one, but this would restrict the hub functionality. Instead, DC circuit breakers could be used to selectively isolate the faulted cable, but relatively few experience has been gained. For the above reasons, the multiple point-to-point HVDC link

structure of Fig. 57 has been preferred in *multiDC*, in which AC cables connect the islands and allow power transfers between onshore grids. A faulted DC cable is isolated by shutting down the corresponding HVDC link.

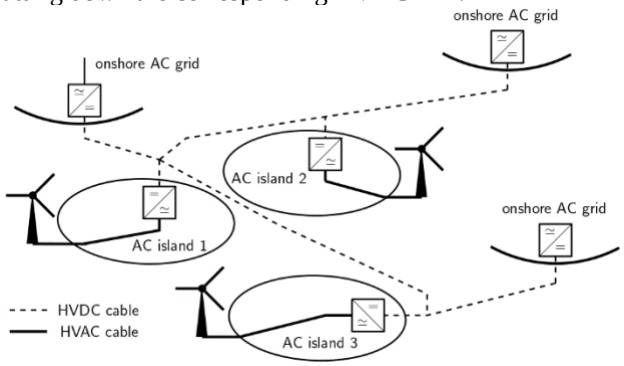

Figure 56. OWPH: the multi-terminal HVDC grid option. Each island could be connected to the HVDC grid through several AC/DC converters (only one per island is shown for clarity).

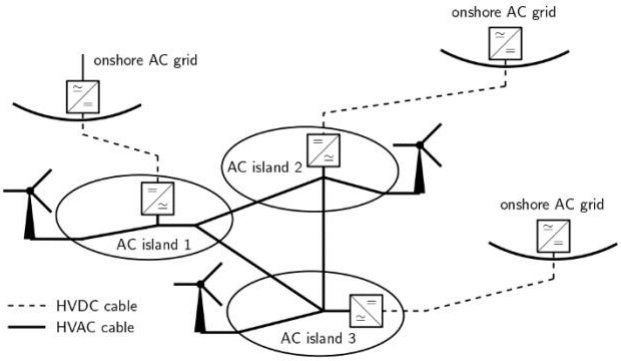

Figure 57. OWPH: the multiple point-to-point HVDC link option. Each island could be connected to onshore grids through several HVDC links (only one per island is shown for clarity).

As the AC islands host wind generators only, VSCs must be used in the HVDC links. The modular multilevel converter (MMC) technology is likely to dominate, for its lower switching losses. With initially no synchronous generator connected to the islands, two approaches are considered, referred to as zero- and low-inertia, respectively.

3) Zero-inertia approach

Zero-inertia obviously refers to the absence of any rotating machine. The offshore VSCs must operate in grid-forming mode. As explained in section V, grid-forming converter-based generators are contemplated as substitutes to the synchronous machines of retired power plants [89]. A variant of grid-forming converters is already used in offshore wind parks connected through an HVDC link; the offshore VSC imposes the magnitude, frequency and phase angle of its terminal voltage. In the OWPH case, however, several high-capacity grid-forming VSCs are connected to the same offshore AC grid. There is thus a need to synchronize them and coordinate their controls. In particular, in the absence of energy storage on the islands, any active power imbalance is quickly corrected by adjusting the power flows in the VSCs, according to the well-known frequency-power droop characteristic. To this purpose, each VSC dynamically adjusts the frequency of its modulated AC voltage in response to the difference between its active power and the reference given by the droop characteristic, as shown in scheme B in section V.C (see Figs. 27 and 29). The VSCs easily synchronize with each other, which results in a steady-state frequency very close to its nominal value.

Each grid-forming VSC behaves as an ideal AC voltage source behind an impedance (in the MMC case, the series impedance of the connection transformer). Therefore, after a large disturbance such as the outage of a wind farm or a DC link, one, several or even all VSCs might switch under current limit [102]. Further investigations are needed to study the impact of such limitations on the offshore grid voltage and frequency, as well as the process by which the VSCs would regain normal (non-limited) operation. The oversizing of some VSCs, to avoid the occurrence of such current limitations, would obviously come at a cost.

4) Low-inertia approach

In the low-inertia approach, the AC islands host synchronous condensers (SCs), as sketched in Fig. 58. Their purpose is twofold: (i) provide a local energy storage, in the form of kinetic energy in the rotating masses; (ii) provide a voltage reference.

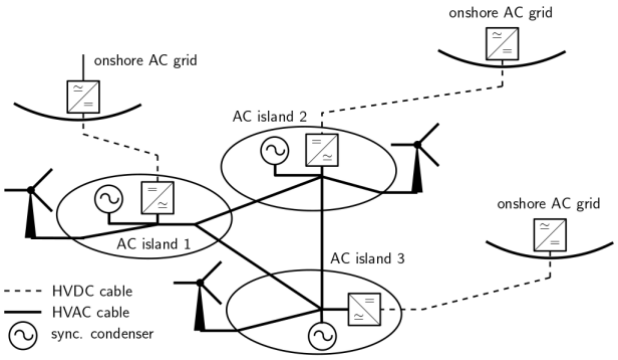

Figure 58. OWPH: low-inertia approach with synchronous condensers (redundant and distributed over the islands).

In this approach, the frequency in the islands is set by the SC rotor speeds. Their kinetic energy storage allows smoothing the impact of offshore disturbances on onshore grids, a feature not readily available in the zero-inertia approach. To illustrate this, consider a sudden drop of the power produced by wind turbines. In the first instants, the missing power is drawn from the kinetic energy of SC rotors, which decelerate. The corresponding frequency decrease is sensed by the VSCs, which in turn decrease their power export to the onshore grids, thereby restoring the balance between wind generator and VSC powers, and stopping the fall of the SC speed. Thus, the SCs act as energy buffers and attenuate offshore disturbances. The drawback of this approach is the

footprint of the additional machines on artificial islands where space can be very limited.

The SCs, equipped with automatic voltage regulators, not only control the grid voltages but also provide a reference with which the VSCs synchronize. Indeed, in this approach, each VSC can operate in grid-following mode (see section V), tracking the grid voltage phasor with a PLL and adjusting the phasor of its injected current in accordance with the desired active and reactive powers.

Following a large disturbance, the grid-following VSCs react as current sources and are less likely to switch under current limit, compared to grid-forming VSCs. In addition, the SCs can tolerate a higher and longer overcurrent than the IGBT-based VSCs. Through an outer control loop each VSC imposes an active power-frequency droop. The frequency deviation left by this control is slowly corrected by a "hub coordinator" with integral action on the frequency error. It can also redistribute the power changes on the various VSCs. There is a clear analogy with standard primary and secondary frequency controls, performed by speed governors and automatic generation control, respectively, although the OWPH dynamics are much faster.

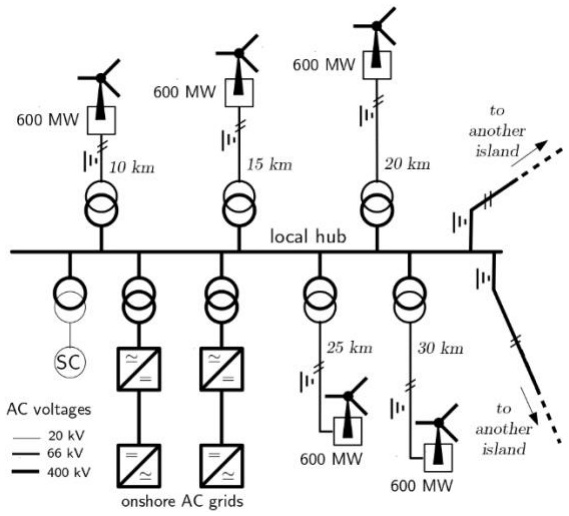

Figure 59. OWPH: single-line diagram of the AC grid of one island

Finally, through another outer control loop, each VSC imposes a reactive power-voltage droop, contributing to voltage control and relieving the SCs.

5) Simulation results

Sample simulation results from the multiDC project are presented hereafter, limited to the low-inertia approach.

The test system includes three islands, as shown in Fig. 58, interconnected through 400-kV cables. The single-line diagram of one island is shown in Fig. 59. The 400-kV "local hub" collects the power of five wind farms through 66-kV cables. Each farm has a capacity of 600 MW and operates in maximum power tracking mode with unity power factor. It is represented by a single aggregate equivalent. Two ± 525-kV HVDC links are connected to the hub through grid-following VSCs with a capacity of 2000 MW each. A SC of 370 MVA nominal apparent power is also connected to the local hub.

The results shown hereafter have been obtained with phasor-mode (or RMS) simulation using the RAMSES software, [124]. This calls for a caveat, in line with the previous sections of this paper. The objective is to adjust the outer control loops (see Section V.A) of the HVDC-link VSCs so as to obtain acceptable damping, settling time and power disturbance attenuation. The focus is on the "slow" dynamics of:

- the synchronous condensers and their excitation systems
- the active and reactive power outer control loops of the HVDC-link VSCs, including their PLLs
- the same for the wind farm equivalents.

The "fast" dynamics of e.g. the cable network, the inner control loops of the wind farms and the HVDC-link VSCs are neglected, i.e. replaced by the corresponding equilibrium equations. To be valid, this simplification requires: (i) the time scales of the fast and slow dynamics to be enough separated, and (ii) the fast dynamics to be stable. The response times chosen for the HVDC-link VSCs are long enough, and the dynamics of wind farms and SCs are slow enough to make assumption (i) acceptable (this could not apply to the fast grid-forming VSCs of the zero-inertia approach). On the other hand, assumption (ii) must be validated on a detailed EMT model of the whole system, for instance to check that no fast mode associated with the cable network is destabilized. Ideally, properly tuned controllers should damp the fast dynamics in such a way that the phasor-mode approximation yields an accurate response of the system over several seconds after a disturbance [125].

The simulations presented next deal with the outage, at t= 1 s, of one of the six HVDC links, initially exporting 1461 MW from island 1. Fig. 60 shows the evolution of the SC rotor speeds. As expected, the HVDC link outage causes a power surplus and, hence, an increase of speed, i.e. of frequency. The hub coordinator brings frequency back to its nominal value in one minute. The overall evolution is not much different from that of a conventional power system, except that the initial rate of change and the maximum deviation of frequency (1.9 Hz) are large. This is due to the low inertia of the SCs. It is not an issue in so far as no load is served by the offshore grid. On the other hand, as mentioned in previous sections, the fast rate of change may limit the validity of some models. It may also require to adjust the wind farm protections. The deviation could be made smaller by a faster control of the VSCs. However, by so doing, the kinetic energy storage would be less exploited and the effects of the outage would propagate faster in onshore grids.

This latter aspect is illustrated by Fig. 61 showing the active power received by the onshore terminal of the other HVDC link connected to island 1. To counteract the offshore power surplus, more power is injected into the onshore grids.

In this example, the hub coordinator shares the total change equally among the five links that remain in operation. The curves refer to different values of the inertia constant H of the SCs (using flywheels for instance). It can be seen that the higher H, i.e. the higher the kinetic energy storage, the smoother the impact of the disturbance.

The voltages of the three local hubs are shown in Fig. 62. The disturbance causes significant but acceptable spikes, after which the voltages are very well controlled. Fig. 63 shows similar spikes in the reactive powers of the three SCs, after which they almost recover to their pre-disturbance values. Indeed, through their reactive power-voltage droop control, the VSCs participate very actively and the excitation systems of the SCs are little solicited.

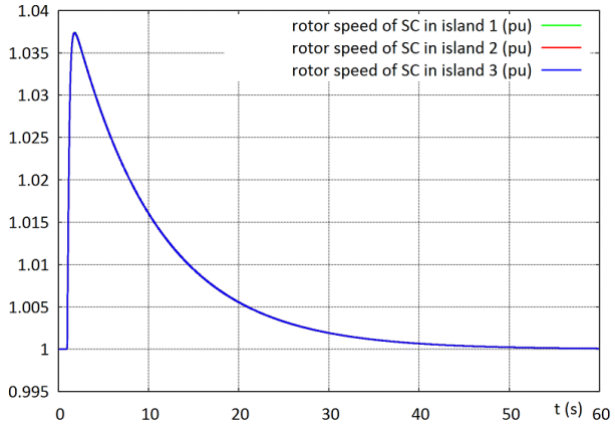

Figure 60. HVDC link outage: SC rotor speeds.

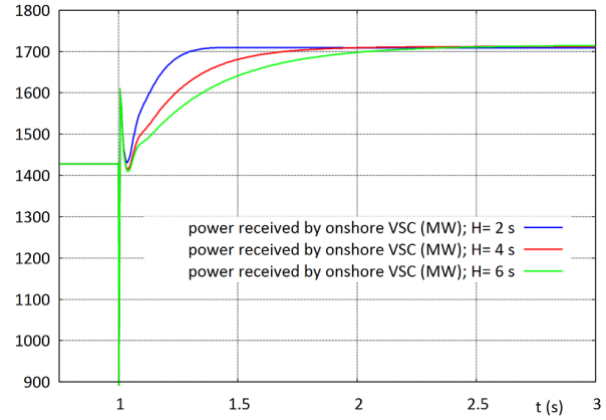

Figure 61. HVDC link outage: power received onshore.

As previously mentioned, the phasor-mode simulation is aimed at rendering the system response over a time interval ranging from a few seconds (see Figs. 61-63) to one minute (see Fig. 60). On the other hand, the spikes observed in Figs. 61 and 62 should be assessed with EMT simulation since they take place significantly faster than the dynamics usually considered in phasor-mode simulation.

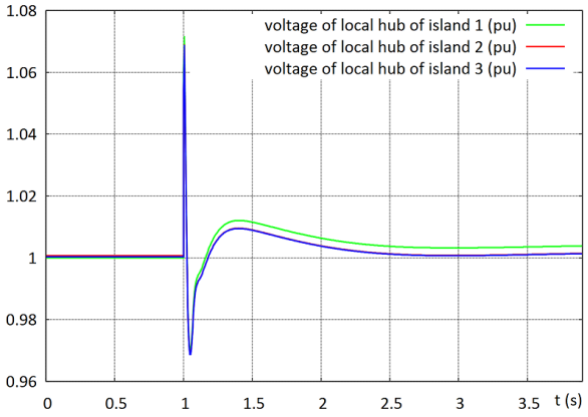

Figure 62. HVDC link outage: voltages at local hubs

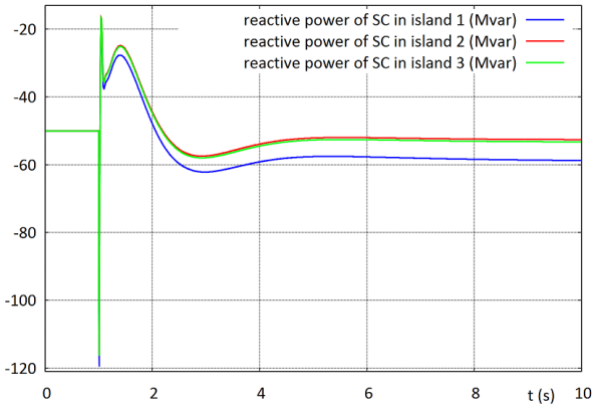

Figure 63. HVDC link outage: reactive powers of SCs

Ongoing comparisons with EMT simulation indicate that the phasor approximation is suitable to reproduce the variations of the active power received by the onshore grids, in response to a rapid rescheduling of the power flowing through the hub or the outage of, respectively, an HVDC link, an offshore AC cable, a whole wind park, or an SC. This is of practical interest for the dynamic security assessment performed by operators of the onshore transmission grids. Indeed, it can hardly be envisaged to simulate an EMT model of the whole system, including the connected onshore grids. For the above-mentioned contingencies, the simulation of that EMT model could be avoided. It would remain indispensable for the simulation of faults in the offshore grid (as it is most likely for faults in the onshore grids near the HVDC link terminals).

The phasor models can also serve a reference for transmission system operators to specify the expected performance (e.g. settling times) of power electronic converters in their grid codes.

VII. Conclusions

Within the context of power grids where a large share of power generation is provided by CIG, the paper has discussed the fundamentals of power systems modelling.

Real-life events discussed in the paper have shown how the usual quasi-sinusoidal (quasi-steady) state of the system may not be necessarily a settled working hypothesis. This has several implications ranging from the simple adoption of phasors to model the physical quantities of the power grid, towards the definition of control functions of CIG and protection schemes. In this respect, the paper has first contextualised the problem of reduced inertia of modern power systems. Then, it has analysed the consequences on voltage/current waveforms exhibiting broad band signals characteristics and discussed the interaction between CIG and synchronous machine's controls. A specific discussion has been provided regarding the behaviour of legacy protection systems and the potential upgrade these systems may need. A large part of the manuscript has been devoted to the discussion of the converters' control as they do represent the main leverage element to be updated in order to guarantee a reliable and stable system dynamics. Clear definitions of grid-following and grid-forming power-electronics-based units have been provided along with a comprehensive classification of these two families of converters' controls.

By relying on open-source simulation models, realistic application examples have been finally illustrated regarding the phasor analysis of power systems experiencing large contingencies as well as the behaviour of different protection and control systems of power grids experiencing high penetration of CIG.

Modelers of power systems dynamics should pay attention when applying (or not) a phasor approximation to study systems characterised by high penetration of CIGs during large disturbances. A benchmark with a corresponding detailed time-domain model may be necessary to compute the detailed behaviour of the CIG and their controls for the purpose of validating the assumptions on both signals and control models. Furthermore, studies are necessary in order to provide modelers with guidelines regarding the use of the phasor approximation vs other types of representation like analytical signals or detailed time-domain models. Finally, it is recommended that power systems operators pay attention when writing grid codes related to systems' controls in the presence of high shares of CIG.

ACKNOWLEDGMENT

The Authors gratefully acknowledge the contributions of Asja Derviškadić, Taoufik Qoria, Ebrahim Rokrok, Roberto Rosso, Rongwu Zhu, Zhiang Zou, Marius Langwasser, Markus Mirz, Bertrand Bastin, Gilles Chaspierre, and Lampros Papangelis.

Furthermore, Authors would like to acknowledge contributions from the multiDC project funded by Innovation Fund Denmark, Grant Agreement No. 6154- 00020B, support from the European Commission through the project SOGNO (GA 774613), PlatOne (GA 864300), the Migrate project funded by European H2020 framework program (GA 691800), the Swiss Centre for Competence in Energy Research on the Future Swiss Electrical Infrastructure (SCCER-FURIES) financially supported by the Swiss Innovation Agency (Innosuisse - SCCER program) as well as the Swiss National Science Foundation via the National Research Programme NRP 70 "Energy Turnaround" and by the Deutsche Forschungsgemeinschaft (DFG, German Research Foundation) via the Priority Programme DFG SPP 1984 "Hybrid and Multimodal Energy Systems".

REFERENCES

[1] IEEE Power System Dynamic Performance Committee, *Contribution to Bulk System Control and Stability by Distributed Energy Resources connected at Distribution Network*, technical report IEEE PES-TR22, Jan. 2017.

[2] ENTSO-E, "Analysis of CE inter-area oscillations of 1st December 2016," European Network of Transmission System Operators for Electricity, Tech. Rep., 2017.

[3] Australian Energy Market Operator (AEMO), "Black System South Australia 28 September 2016," technical report, March, 2017.

[4] Australian Energy Market Operator (AEMO), "Final report- Queensland and South Australia system separation on 25 August 2018", technical report, 2019.

[5] R. Lasseter, Z. Chen and D. Pattabiraman, "Grid-Forming Inverters: A Critical Asset for the Power Grid," *IEEE Journal of Emerging and Selected Topics in Power Electronics* (accepted, in press).

[6] P. Tielens and D. Van Hertem, "The relevance of inertia in power systems," Renewable and Sustainable Energy Reviews, vol. 55, pp. 999–1009, 2016.

[7] D. Groß and F. Döfler, "On the steady-state behavior of low-inertia power systems," *20th IFAC World Congress*, vol. 50, no. 1, pp. 10 735 – 10 741, 2017.

[8] F. Milano, F. Dörfler, G. Hug, D. Hill, G. Verbic, "Foundations and Challenges of Low-Inertia Systems", *Proc. of the 20th Power Systems Computation Conference* (PSCC), 2018.

[9] J. Jia, G. Yang and A. H. Nielsen, "A Review on Grid-Connected Converter Control for Short-Circuit Power Provision Under Grid Unbalanced Faults," *IEEE Transactions on Power Delivery*, vol. 33, no. 2, pp. 649-661, April 2018.

[10] J. Fang, Y. Tang, H. Li and F. Blaabjerg, "The Role of Power Electronics in Future Low Inertia Power Systems," *Proc. of the 2018 IEEE International Power Electronics and Application Conference and Exposition (PEAC)*, Shenzhen, 2018.

[11] D. Shu , X. Xie , H. Rao, X. Gao, Q. Jiang, Y. Huang "Sub- and Super-Synchronous Interactions between STATCOMs and weak AC/DC Transmissions with series compensations," *IEEE Transaction on Power Electronics*, vol. 33, n.4, 2018.

[12] W. Liu, Z. Lu, X. Wang, X. Xie "Frequency-coupled admittance modelling of grid-connected voltage source converters for the stability evaluation of subsynchronous interaction," *IET Renewable Power Generation*, vol.13, n. 2, 2019

[13] Y. Li, L. Fan, Z. Miao, "Wind in Weak Grids: Low-Frequency Oscillations, Subsynchronous Oscillations, and Torsional Interactions" *IEEE Transaction on Power Systems*, vol. 35, n. 1, 2020.

[14] Z. Wu et al., "State-of-the-art review on frequency response of wind power plants in power systems," *Journal of Modern Power Systems and Clean Energy*, vol. 6, no. 1, pp. 1-16, Jan. 2018.

[15] M. Rezkalla, M. Pertl, M. Marinelli, "Electric power system inertia: requirements, challenges and solutions", Electrical Engineering, vol. 100, pp- 2677–2693, 2018.

[16] P. Tielens and D. Van Hertem, "The relevance of inertia in power systems," *Renewable and Sustainable Energy Reviews*, vol. 55, pp. 999-1009, March 2016.

[17] J. Fang, H. Li, Y. Tang and F. Blaabjerg, "On the Inertia of Future More-Electronics Power Systems," in IEEE Journal of Emerging and Selected Topics in Power Electronics, vol. 7, no. 4, pp. 2130-2146, Dec. 2019.

[18] G. Tsourakis, S. Nanou, C. Vournas, "A Power System Stabilizer for Variable-Speed Wind Generators", *Proc. of the 18th IFAC World Congress*, Milan, Italy, Aug/Sept 2011.

[19] *Modeling and Dynamic Behavior of Wind Generation as it Relates to Power System Control and Dynamic Performance*, CIGRE Technical Report 328, Aug. 2007.

[20] J. Morren, S.W.H. de Haan, W.L. Kling, J.A. Ferreira, "Wind turbines emulating inertia and supporting primary frequency control", *IEEE Transactions on Power Systems*, vol.21, n. 1, pp. 433-434, Feb. 2006.

[21] G. Lalor, A. Mullane, M.J. O' Malley, "Frequency Control and wind turbine technologies", *IEEE Transactions on Power Systems*, vol. 20, n. 4, pp. 1905-1913, Nov. 2005.

[22] D. Gautam, L. Goel, R. Ayyanar, V. Vittal, T. Harbour, "Control Strategy to Mitigate the Impact of Reduced Inertia Due to Doubly Fed Induction Generators on Large Power Systems", *IEEE Transactions on Power Systems*, vol. 26, n. 1, pp. 214-224, Feb. 2011.

[23] L. N. Papangelis, C. D. Vournas, "Design Principles of Wind Turbine Inertia Emulators for Autonomous Systems", *Proc of the 19th IFAC World Congress*, Cape Town, Aug. 2014.

[24] *ENTSO-E Guidance document for national implementation for network codes on grid connection*, High Penetration of Power Electronic Interfaced Power Sources (HPoPEIPS)– March 2017.

[25] D. Raisz, A. Musa, F. Ponci and A. Monti, "Linear and Uniform Swing Dynamics," *IEEE Transactions on Sustainable Energy*, vol. 10, no. 3, pp. 1513-1522, July 2019.

[26] A. Derviškadić, G. Frigo and M. Paolone "Beyond Phasors: Modeling of Power System Signals Using the Hilbert Transform", *in IEEE Trans. on Power Systems* (accepted, in press).

[27] M. Vetterli, J. Kovačević, and V. K. Goyal, *Foundations of Signal Processing*. Cambridge University Press, Cambridge, 2014.

[28] H. Kirkham A. Riepnieks, M. Albu, and D. Laverty, "The Nature of Measurement, and the True Value of a Measured Quantity," in IEEE Int. Instr. and Meas. Conf (I2MTC), Houston, USA, 2018, doi: 10.1109/I2MTC.2018.8409771.

[29] H. Kirkham, and D.R. White, "Reactive Power and GIC: The Problems of an Unrecognized Operationalist Measurement," in IEEE 9th Int. Workshop on Appl. Meas. for Power Systems (AMPS), Bologna, Italy, 2018, doi: 10.1109/AMPS.2018.8494870.

[30] NEMA, "Definitions for Calculations of VA, VAh, VAR, and VARh for Poly-Phase Electricity Meters," NEMA C12.24 TR-2011, National Electrical Manufacturers Association, Rosslyn, VA, USA, 2011.

[31] IEEE Standard Definitions for the Measurement of Electric Power Quantities under Sinusoidal, Nonsinusoidal, Balanced, or Unbalanced Conditions, IEEE Standard 1459-2010.

[32] M. Malengret, C.T. Gaunt, "General theory of average power for multi-phase systems with distortion, unbalance and direct current components. *Electrical Power Systems Research*, vol. 84, pp. 224-230, 2011.

[33] M. Malengret, and C.T. Gaunt, "Inverters and Compensators for Minimum Line Losses," *Prof. of the Int. Conf. on Power Electron. and Appl. and Exhibition* (EPE), Karlsruhe, Germany, 2016.

[34] H. Lev-Ari, R. D. Hernández, A. M. Stanković, and E. A. Marengo, "Adaptive Near-Optimal Compensation in Lossy Polyphase Power Systems," *IEEE Transactions on Control Systems Technonogies*, vol. 26, no. 2, pp. 732-739, 2018.

[35] M. Malengret, C.T. Gaunt, "General Frequency-Domain Derivation of Active Currents and Power Factor at any Multi-Wire Point of Connection in a Network", unpublished, submitted for review, 2019.

[36] Gefei Kou, Le Chen, P. VanSant, F. Velez-Cedeno and Yilu Liu, "Fault Characteristics of Distributed Solar Generation", *IEEE Transactions on Power Delivery*, Volume 35, Issue 2, pp 1062-1064, April 2020.

[37] I. Erlich, T. Neumann, F. Shewarega, P. Schegner and J. Meyer, "Wind turbine negative sequence current control and its effect on power system protection", *Proceedings of the IEEE PES General Meeting*, July 2013, pp. 1-5.

[38] M. Nagpal and C. Henville, "Impact of power-electronic sources on transmission line ground fault protection", *IEEE Transactions on Power Delivery*, Vol. 33, No. 1, pp. 62-70, February 2018.

[39] A. Haddadi, I. Kosar, U. Karaagac, H. Gras and E. Farantatos, "Impact of wind generation on power swing protection", *IEEE Transactions on Power Delivery*, Vol. 34, No. 3, pp. 1118-1128, June 2019.

[40] EPRI Technical Brief, *Impact of Inverter-Based Resources on Protection Schemes Based on Negative Sequence Components*.

[41] A. P. Meliopoulos, M. Kezunovic, G. Karady, "Grid Transformation: Setting-less Protection Methods", PSERC White Paper, 2012.

[42] A C Westrom, A. P. S. Meliopoulos, G. J. Cokkinides, *Method and Apparatus for Detecting and Responding to Downed Conductors*, U.S. Patent #5,341,265, August 23, 1994.

[43] S. Bhattacharya, "Power system protection problems caused by grid connected PV systems" thesis, the University of Queensland, 2014.

[44] H. L. R. Walt, R. C. Bansal, and R. Naidoo "PV based distributed generation power system protection: A review," *Renewable Energy Focus*, vol. 24, pp. 33-40, 2018.

[45] A. Sinclair, D. Finney, D. Martin, and P. Sharma, "Distance protection in distribution systems: How it assists with integrating distributed resources," *IEEE Transactions on Ind. Appl.*, vol. 50, no. 3, pp. 2186_2196, May 2014.

[46] V. C. Nikolaidis, A. M. Tsimtsios, and A. S. Safigianni "Investigating particularities of infeed and fault resistance effect on distance relays protecting radial distribution feeders with DG," *IEEE Access*, 2018.

[47] P. Mahat, Z. Chen, B. Bak-Jensen, and C. L. Bak "A simple adaptive overcurrent protection of distribution systems with distributed generation", *IEEE Transactions on Smart Grid*, vol.2, no.3, 2011.

[48] R. Moxley, and K. Fodero "High-Speed Distribution Protection Made Easy: Communications-Assisted Protection Schemes for Distribution Applications" *SEL Journal of Reliable Power*, vol.3, no. 2, 2012.

[49] H. L. Gao, J. Li, and B.Y. Xu, "Principle and implementation of current differential protection in distribution networks with high penetration of DGs," *IEEE Transactions on Power Delivery*, vol. 32, no. 1, pp. 565–574, 2017.

[50] M. Farrokhabadi et al., "Microgrid Stability Definitions, Analysis, and Examples," *IEEE Transactions on Power Systems*, vol. 35, no. 1, pp. 13-29, Jan. 2020.

[51] X. Wang and F. Blaabjerg, "Harmonic Stability in Power Electronic-Based Power Systems: Concept, Modeling, and Analysis," *IEEE Transactions on Smart Grid*, vol. 10, no. 3, pp. 2858-2870, May 2019.

[52] N. Bottrell, M. Prodanovic and T. C. Green, "Dynamic Stability of a Microgrid With an Active Load," *IEEE Transactions on Power Electronics*, vol. 28, no. 11, pp. 5107-5119, Nov. 2013.

[53] R. Rosso, M. Andresen, S. Engelken, and M. Liserre, "Analysis of the interaction among power converters through their synchronization mechanism," *IEEE Transactions on Power Electronics*, vol. 34, no. 12, pp. 12321-12332, Dec. 2019.

[54] Z. Zou, R. Rosso and M. Liserre, "Modeling of the Phase Detector of a Synchronous-Reference-Frame Phase-Locked Loop based on Second-Order Approximation," *IEEE Journal of Emerging and Selected Topics in Power Electronics*, accepted, in press, 2020

[55] H. Yuan, X. Yuan and J. Hu, "Modeling of Grid-Connected VSCs for Power System Small-Signal Stability Analysis in DC-Link Voltage Control Timescale," *IEEE Transactions on Power Systems*, vol. 32, no. 5, pp. 3981-3991, Sept. 2017.

[56] G. De Carne et al., "Which Deepness Class Is Suited for Modeling Power Electronics? A Guide for Choosing the Right Model for Grid-Integration Studies," *IEEE Industrial Electronics Magazine*, vol. 13, no. 2, pp. 41-55, June 2019.

[57] Z. Zou, G. Buticchi, M. Liserre, A. M. Kettner and M. Paolone, "Voltage stability analysis using a complete model of grid-connected voltage-source converters," *IEEE Energy Conversion Congress and Exposition (ECCE)*, Milwaukee, WI, 2016.

[58] NGESO, "Expert workgroup on fast fault current injection - terms of reference," https://www.nationalgrideso.com

[59] R. Rosso, S. Engelken and M. Liserre, "Robust Stability Investigation of the Interactions Among Grid-Forming and Grid-Following converters," *IEEE Journal of Emerging and Selected Topics in Power Electronics*, accepted in press, 2020.

[60] R. Rosso, J. Cassoli, G. Buticchi, S. Engelken, and M. Liserre, "Robust stability analysis of LCL filter based synchronverter under different grid conditions," *IEEE Transactions on Power Electronics*, vol. 34, no. 6, pp. 5842-5853, June 2019.

[61] T. Qoria, F. Gruson, F. Colas, G. Denis, T. Prevost, and X. Guillaud, "Inertia effect and load sharing capability of grid-forming converters connected to a transmission grid," *Proc. of the 15th IET International Conference on AC and DC Power Transmission (ACDC 2019)*, 2019.

[62] R. Rosso, S. Engelken and M. Liserre, "Robust Stability Analysis of Synchronverters Operating in Parallel," *IEEE Transactions on Power Electronics*, vol. 34, no. 11, pp. 11309-11319, Nov. 2019.

[63] M. G. Taul, X. Wang, P. Davari and F. Blaabjerg, "Current Limiting Control with Enhanced Dynamics of Grid-Forming Converters during Fault Conditions," *IEEE Journal of Emerging and Selected Topics in Power Electronics*, accepted in press, 2020.

[64] R. Rosso, S. Engelken, and M. Liserre, "Current limitation strategy for grid-forming converters under symmetrical and asymmetrical grid faults," *IEEE Energy Conversion Congress and Exposition (ECCE)*, to appear, 2020.

[65] PSC Specialist Consultants to the Electricity industry, "Review of AEMO's PSCAD Modelling of the Power System in South Australia," technical report, 22 December 2017.

[66] Australian Energy Market Operator (AEMO), "Response of existing PV inverters to frequency disturbances", technical report, April 2016.

[67] NERC Disturbance Report, "1,200 MW Fault Induced Solar Photovoltaic Resource Interruption Disturbance Report", June 2017.

[68] Joint NERC and WECC Staff Report, "900 MW Fault Induced Solar Photovoltaic Resource Interruption Disturbance Report", February 2018.

[69] U. Markovic, O. Stanojev, E. Vrettos, P. Aristidou and G. Hug, "Understanding Stability of Low-Inertia Systems", EnergXiv, available on-line https://doi.org/10.31224/osf.io/jwzrq, Feb. 2019.

[70] A.V. Oppenheim, R.W. Schafer, J.R. Buck, et al., *Discrete-Time Signal Processing*, vol. 2. Englewood Cliffs, NJ: Prentice-Hall, 1989.

[71] D. Macii, D. Fontanelli, G. Barchi, and D. Petri, "Impact of acquisition wideband noise on synchrophasor measurements: A design perspective," *IEEE Transactions on Instrumentation and Measurement*, vol. 65, pp. 2244–2253, Oct. 2016.

[72] *IEEE/IEC International Standard - Measuring relays and protection equipment – Part 118-1: Synchrophasor for power systems - Measurements*, IEC/IEEE 60255-118-1:2018, pp. 1–78, Dec. 2018.

[73] A. Derviškadić, "Synchronized Sensing for Wide-Area Situational Awareness of Electrical Grids in Non-Stationary Operating Conditions," PhD Disseration, Ecole Polytechnique Fédérale de Lausanne, Switzerland, 2019.

[74] *IEC Std 61000-4-7:2002(E), Part 4-7: Testing and Measurement Techniques – General Guide on Harmonics and Interharmonics Measurements and Instrumentation, for Power Supply Systems and Equipment Connected Thereto*, 2002.

[75] J. Mahseredjian et al., "On a new approach for the simulation of transients in power systems," *Electric Power Systems Research*, vol. 77, no. 11, 2007.

[76] P. Romano and M. Paolone, "Enhanced Interpolated-DFT for Synchrophasor Estimation in FPGAs: Theory, Implementation and Validation of a PMU Prototype", *IEEE Trans. on Instrumentation and Measurements*, vol. 63, num. 12, pp. 2824 - 2836, Dec. 2014

[77] S. L. Hahn, *Hilbert transforms in signal processing*. Artech House, 1996.

[78] S. R. Sanders, J. M. Noworolski, X. Z. Liu, et al., "Generalized averaging method for power conversion circuits", *IEEE Transactions on Power Electronics*, vol. 6, no. 2, pp. 251–259, 1991.

[79] A. M. Stankovic, B. C. Lesieutre, and T. Aydin, "Modeling and analysis of single-phase induction machines with dynamic phasors", *IEEE Transactions on Power Systems*, vol. 14, no. 1, pp. 9–14, 1999.

[80] A. M. Stankovic and T. Aydin, "Analysis of asymmetrical faults in power systems using dynamic phasors", *IEEE Transactions on Power Systems*, vol. 15, no. 3, pp. 1062–1068, 2000.

[81] B. S. Munir, M. Reza, A. Trisetyarso and B. S. Abbas, "Feature extraction using Hilbert-Huang transform for power system oscillation measurements," *Proc. of the 4th International Conference on Information Technology, Computer, and Electrical Engineering (ICITACEE)*, Semarang, 2017, pp. 93-96.

[82] M. Mirz, A. Estebsari, F. Arrigo, et al., "Dynamic phasors to enable distributed real-time simulation", *Proc. of the 6th IEEE International Conference on Clean Electrical Power (ICCEP)*, pp. 139–144, 2017.

[83] H. W. Dommel, "Digital computer solution of electromagnetic transients in single-and multiphase networks", *IEEE Transactions on Power Apparatus and Systems*, vol. PAS-88, no. 4, pp. 388–399, Apr. 1969.

[84] FEIN Aachen e.V. (Accessed 2018-11-23). DPsim, available online: https://www.fein-aachen.org/projects/dpsim/

[85] M. Mirz, S. Vogel, G. Reinke, and A. Monti, "DPsim — A dynamic phasor real-time simulator for power systems", *SoftwareX*, vol. 10, p. 100253, 2019.

[86] *Cigré Benchmark Systems for Network Integration of Renewable and Distributed Energy Resources*. Available online: http://www.e-cigre.org/publication/575-benchmark-systems-for-network-integration-of-renewable-and-distributed-energy-resources.

[87] J. Rocabert, A. Luna, F. Blaabjerg, and P. Rodríguez, "Control of Power Converters in AC Microgrids," *IEEE Transactions on Power Electronics*., vol. 27, no. 11, pp. 4734–4749, Nov. 2012.

[88] A.D. Paquette, M.J. Reno, R.G. Harley, and D.M. Divan, "Sharing Transient Loads : Causes of Unequal Transient Load Sharing in Islanded Microgrid Operation," *IEEE Ind. Appl. Mag.*, vol. 20, no. 2, pp. 23–34, Mar. 2014.

[89] J. Matevosyan et al., "Grid-forming inverters", *IEEE Power and Energy magazine*, Nov./Dec. 2019, pp. 89-98

[90] P. Unruh , M. Nuschke, P. Strauß, F. Welck " Overview on grid-forming inverter control methods", *Energies*, vol. 13, 2589, n. 10, 2020.

[91] E. Rokrok, T. Qoria, A. Bruyere, B. Francois, and X. Guillaud, "Effect of Using PLL-Based Grid-Forming Control on Active Power Dynamics Under Various SCR," *Proc. of the 45th Annual Conference of the IEEE Industrial Electronics Society (IECON)*, pp. 4799–4804, 2019.

[92] E. Rokrok, T. Qoria, A. Bruyere, B. Francois, and X. Guillaud, "Classification and Dynamic Assessment of Droop- Based Grid-Forming Control Schemes: Application in HVDC Systems," *Proc. of the 21st Power Systems Computation Conference*, 2020.

[93] S. D'Arco, J. A. Suul, and O. B. Fosso, "A Virtual Synchronous Machine implementation for distributed control of power converters in SmartGrids," *Electrical Power Systems Research*, vol. 122, pp. 180–197, May 2015.

[94] H. Beck and R. Hesse, "Virtual synchronous machine," *Proc. of the 9th International Conference on Electrical Power Quality and Utilisation*, 2007.

[95] H2020 Migrate Project, WP3, "Control and Operation of a Grid with 100 % Converter-Based Devices", Deliverable 3.2, Local control and simulation tools for large transmission systems," available online: https://www.h2020-migrate.eu/

[96] L. Zhang, L. Harnefors, and H.-P. Nee, "Power-Synchronization Control of Grid-Connected Voltage-Source Converters," *IEEE Transactions on Power Systems*, vol. 25, no. 2, pp. 809–820, May 2010.

[97] T. Qoria, F. Gruson, F. Colas, X. Guillaud, M. S. Debry, and T. Prevost, "Tuning of cascaded controllers for robust grid-forming voltage source converter," *Proc. of the 20th Power Systems. Computation Conference*, 2018.

[98] T. Qoria, C. Li, K. Oue, F. Gruson, F. Colas, and X. Guillaud, "Direct AC voltage control for grid - forming inverters," *Journal of Power Electronics*, no. 0123456789, 2019.

[99] J. Zhou, D. Hui, S. Fan, Y. Zhang, and A. M. Gole, "Impact of shortcircuit ratio and phase-locked-loop parameters on the small-signal behavior of a VSC-HVDC converter," *IEEE Transactions on Power Delivery*, vol. 29, no. 5 pp. 2287–2296, Oct. 2014.

[100] A. Adib, B. Mirafzal, X. Wang and F. Blaabjerg, "On Stability of Voltage Source Inverters in Weak Grids," *IEEE Access*, vol. 6, pp. 4427-4439, 2018.

[101] M. Yu et al., "Use of an inertia-less Virtual Synchronous Machine within future power networks with high penetrations of converters," *Proc. of the 19th Power Systems Computation Conference*, 2016.

[102] T. Qoria, F. Gruson, F. Colas, X. Guillaud, "Current Limiting Algorithms and Transient Stability Analysis of Grid-Forming VSCs," *Proc. of the 21st Power Systems Computation Conference (PSCC)*, 2020.

[103] https://github.com/l2ep-epmlab/

[104] https://www.h2020-migrate.eu/downloads.html

[105] C. Arghir F. Dörfler "The Electronic Realization of Synchronous Machines: Model Matching Angle Tracking, and Energy Shaping Techniques," *IEEE Transaction on Power Electronics*, vol. 35, n. 4, April 2020.

[106] G. Seo, M. Colombino, I. Subotic, B. Johnson, D. Gross, F. Dorfler "Dispatchable Virtual Oscillator Control for Decentralized Inverter-dominated Power Systems: Analysis and Experiments", *Proc. of the IEEE APEC*, 2019.

[107] IEEE-39-bus-power-system model, available open-source at https://github.com/DESL-EPFL/IEEE-39-bus-power-system
[108] S. Meliopoulos, G. J. Cokkinides, P. Myrda, Yu Liu, Rui Fan, Liangyi Sun, Renke Huang and Zhenyu Tan, "Dynamic State Estimation Based Protection: Status and Promise", *IEEE Transactions on Power Delivery*, vol. 32, no. 1, pp 320-328, Feb. 2017.
[109] Sungyun Choi and A. P. S. Meliopoulos, "Effective Real-time Operation and Protection Scheme of Microgrids Using Distributed Dynamic State Estimation", *IEEE Transactions on Power Delivery*, vol. 32, no. 1, pp 504-514, June 2016.
[110] Yu Liu, A. P. Meliopoulos, Rui Fan, Liangyi Sun, and Zhenyu Tan, "Dynamic State Estimation Based Protection on Series Compensated Transmission Lines", *IEEE Transactions on Power Delivery*, vol. 32, no. 5, pp. 2199-2209, Oct. 2017.
[111] Yu Liu, A. P. Meliopoulos, Liangyi Sun, and Rui Fan, "Dynamic State Estimation Based Protection of Mutually Coupled Transmission Lines", *CSEE Journal of Power and Energy Systems*, Vol. 2, Issue: 4, pp 6-14, Dec. 2016.
[112] Yu Liu, A P S. Meliopoulos, Zhenyu Tan, Liangyi Sun, and Rui Fan, "Dynamic State Estimation Based Fault Locating on Transmission Lines", *IET Generation, Transmission & Distribution*, 9 pp, DOI: 10.1049/iet-gtd.2017.0371, June 2017.
[113] Hussain F. Albinali and A. P. Meliopoulos, "Resilient Protection System through Centralized Substation Protection", *IEEE Transactions on Power Delivery*, vol. 33, no. 3, pp 1418-1427, June 2018.
[114] Yu Liu, G. Ramos, and A. P. Meliopoulos, "Comparison of Transformer Legacy Protective Functions and a Dynamic State Estimation-Based Approach", *Electric Power Systems Research*, accepted, 2020.
[115] P. M. Anderson and A. A. Fouad, *Power System Control and Stability*. IEEE Press, 2003.
[116] D. Ramasubramanian, Z. Yu, R. Ayyanar, V. Vittal, and J. Undrill, "Converter Model for Representing Converter Interfaced Generation in Large Scale Grid Simulations," *IEEE Transactions on Power Systems*, Vol. 32, No. 1, pp. 765-773, January 2017.
[117] D. Ramasubramanian, "Impact of Converter Interfaced Genration and Load on Grid Performance," PhD Disseration, Arizona State University, 2017.
[118] PSLF, GE Energy Consulting, http://www.geenergyconsulting.com/practice-area/software-products/pslf
[119] D. Ramasubramanian, V. Vittal, J. Undrill, "Transient Stability Analysis of an all Converter Interfaced Generation WECC System," *19th Power Systems Computation Conference*, Genoa, Italy, June 20-24, 2016.
[120] European Commission, "Political Declaration on energy cooperation between the North Seas Countries," Jun. 2016.
[121] E. Ruijgrok, E. van Druten and B. Bulder, "Cost Evaluation of North Sea Offshore Wind Post 2030," North Sea Wind Power Hub - Consortium Partners, Devender, Netherlands, 2019.
[122] F. Thams, R. Eriksson and M. Molinas, "Interaction of Droop Control Structures and its Inherent Effect on the Power Transfer Limits in Multi-terminal VSC-HVDC," *IEEE Transactions on Power Delivery*, vol. 32, no. 1, pp. 182 - 192, 2016.
[123] K. Bell, L. Xu, T.Houghton, "Considerations in design of an offshore network", *CIGRE Science & Engineering*, vol.1, pp. 79-92, Feb. 2015.
[124] P. Aristidou, D. Fabozzi, and T. Van Cutsem, "Dynamic Simulation of Large-Scale Power Systems Using a Parallel Schur-Complement-Based Decomposition Method," *IEEE Transactions on Parallel and Distributed Systems*, vol. 25, no. 10, pp. 2561–2570, 2014.
[125] G. Misyris, S. Chatzivasileiadis, T. Weckesser, "Zero-Inertia Systems: Sufficient Conditions for Phasor Modeling," available online: https://arxiv.org/abs/2002.11209, 2020.